

UNIVERSIDADE FEDERAL DO RIO GRANDE DO SUL
INSTITUTO DE INFORMÁTICA
PROGRAMA DE PÓS-GRADUAÇÃO EM COMPUTAÇÃO

MATHEUS LUAN KRUEGER

**Visual Simulation of Refractive Errors on
Monochromatic Images
and
An Empirical Evaluation of the Absolute
Threshold for Vision**

Thesis presented in partial fulfillment
of the requirements for the degree of
Master of Computer Science

Advisor: Prof. Dr. Manuel Menezes de Oliveira Neto

Porto Alegre
July 2015

CIP — CATALOGING-IN-PUBLICATION

Krueger, Matheus Luan

Visual Simulation of Refractive Errors on Monochromatic Images

and

An Empirical Evaluation of the Absolute Threshold for Vision /
Matheus Luan Krueger. – Porto Alegre: PPGC da UFRGS, 2015.

79 f.: il.

Thesis (Master) – Universidade Federal do Rio Grande do Sul.
Programa de Pós-Graduação em Computação, Porto Alegre, BR–RS, 2015. Advisor: Manuel Menezes de Oliveira Neto.

1. Low-order aberrations. 2. Fourier optics. 3. PSF. 4. Absolute threshold. I. Oliveira Neto, Manuel Menezes de. II. Título.

UNIVERSIDADE FEDERAL DO RIO GRANDE DO SUL

Reitor: Prof. Carlos Alexandre Netto

Vice-Reitor: Prof. Rui Vicente Oppermann

Pró-Reitor de Pós-Graduação: Prof. Vladimir Pinheiro do Nascimento

Diretor do Instituto de Informática: Prof. Luis da Cunha Lamb

Coordenador do PPGC: Prof. Luigi Carro

Bibliotecária-chefe do Instituto de Informática: Beatriz Regina Bastos Haro

*This thesis is dedicated to my parents,
Marcilio Krueger and Ruth Matias Krueger,
for their support, trust and unconditional love.*

ACKNOWLEDGMENTS

This journey would not have been possible without the support of my family, professors and mentors, and friends. I would like to thank my family, for encouraging me in all of my pursuits and inspiring me to follow my dreams. To my friends, thank you for supporting and helping me over the years. I am also grateful to Manuel Menezes de Oliveira Neto e Airton Leite Kronsauer, my mentors, for their sincere and valuable guidance along this journey.

I take this opportunity to express my gratitude to Fundação de Amparo à Pesquisa do Estado do Rio Grande do Sul (FAPERGS) and Coordenação de Aperfeiçoamento de Pessoal de Nível Superior (CAPES) for financial support. I also place on record, my sense of gratitude to one and all, who directly or indirectly, have lent their ‘eyes’ in this venture.

ABSTRACT

We present a practical approach for simulating the perception of monochromatic images considering optical systems with low-order aberrations (*i.e.*, myopia, hyperopia and astigmatism). It uses Fourier Optics and a DSLR camera to simulate and validate results of how such aberrations affect vision. We demonstrate its effectiveness by comparing the simulation outcomes with an optical ground truth with three objective metrics. In addition to simulation, we present a psychophysical study about the visual absolute threshold, suggesting its applicability in order to discover the spherical equivalent. Preliminary evaluation has shown that our technique produces convincing results.

Keywords: Low-order aberrations. Fourier optics. PSF. Absolute threshold.

Simulação da percepção visual de imagens monocromáticas considerando aberração de baixa ordem e um estudo sobre o mínimo visível

RESUMO

Esta dissertação apresenta uma abordagem prática para o problema de simulação da percepção de imagens monocromáticas considerando sistemas ópticos com aberrações de baixa ordem (miopia, hipermetropia e astigmatismo). Nossa técnica utiliza óptica de Fourier e uma câmera DSLR para simular e validar os resultados de como as aberrações afetam a visão. Nós demonstramos a sua eficácia utilizando três métricas objetivas de comparação entre os resultados da simulação e imagens capturadas por uma câmera simulando o mesmo nível de aberração. Além da simulação, também apresentamos um estudo psicofísico a respeito do mínimo visível, sugerindo a sua aplicabilidade para se descobrir o equivalente esférico. Uma avaliação preliminar mostra que nossa técnica produz resultados convincentes.

Palavras-chave: Aberrações de baixa ordem, Óptica de Fourier, PSF, Mínimo visível.

LIST OF FIGURES

Figure 1.1 The human eye and some low-order aberrations	17
Figure 1.2 A real scene with objects at different depths	19
Figure 2.1 General flow of sensory information	21
Figure 2.2 The Electromagnetic Spectrum and Visible Light.....	22
Figure 2.3 Human Senses: organs, energy stimuli, and sensory receptors	23
Figure 2.4 Construction of the optotype E.....	24
Figure 2.5 Parts of the Eye	25
Figure 2.6 The unit circle	26
Figure 2.7 Zernike terms expansion pyramid.....	28
Figure 2.8 General concepts of wavefront	29
Figure 3.1 Overview of the vision-realistic rendering algorithm	31
Figure 3.2 Yu (2001) uses data captured using a Shack-Hartmann aberrometer (a) to simulate blur at specific depth values (b) and (c).	32
Figure 3.3 The temporal glare pipeline	33
Figure 4.1 A roadmap for Fourier optics	35
Figure 4.2 Standard Sloan Letters.....	36
Figure 4.3 LogMAR Charts	37
Figure 4.4 Example of a normalized Wavefront map	39
Figure 4.5 Optical systems used in the validation process.....	41
Figure 4.6 Vertex distance and our optical setup	41
Figure 4.7 Myopic perception of 20/200 Sloan black letters.....	44
Figure 4.8 Myopic perception of 20/200 Sloan white letters.....	45
Figure 4.9 Hyperopic perception of 20/200 Sloan black letters	46
Figure 4.10 Hyperopic perception of 20/200 Sloan white letters	47
Figure 4.11 Astigmatic perception of 20/200 Sloan black letters (-2@ 90)	48
Figure 4.12 Astigmatic perception of 20/200 Sloan black letters (-2@ 180)	49
Figure 4.13 Astigmatic perception of 20/200 Sloan black letters (+2@ 90)	50
Figure 4.14 Astigmatic perception of 20/200 Sloan black letters (+2@ 180)	51
Figure 4.15 Myopic perception of 20/200 Sloan black letters	52
Figure 4.16 Myopic perception of 20/200 Sloan white letters.....	53
Figure 4.17 Simulations with arbitrary wavefronts.....	54
Figure 5.1 Geometrical perspective of the circle of confusion	57
Figure 5.2 Absolute Threshold Experiment stages	59
Figure 5.3 Apparatus designed to help in the absolute threshold psychophysical evaluations	61
Figure 5.4 XXX.....	61
Figure 5.5 XXX.....	62
Figure 5.6 Variations of the apparatus	63
Figure 5.7 Plot of absolute threshold data acquired with and without eyedrops	63
Figure 5.8 Accommodation analysis.....	64
Figure 5.9 Polynomial fitting of the absolute threshold values of Subject 1	65
Figure 5.10 Polynomial fitting of the absolute threshold values of Subject 11	66
Figure 6.1 Histogram of SSIM and PSNR	67

LIST OF TABLES

Table 2.1 Sensory threshold of five senses.....	23
Table 2.2 Zernike polynomials up to the fifth order.....	27
Table 4.1 Camera apertures and pupil diameters for various f-numbers.	40
Table 4.2 Actual increase in dioptic power obtained by placing additional lenses with various powers in front of the camera's main lens considering a vertex distance of 10mm.	42
Table 4.3 SSIM and PSNR table of myopic perception (Figure 4.7).....	44
Table 4.4 SSIM and PSNR table of myopic perception (Figure 4.8).....	45
Table 4.5 SSIM and PSNR table of hyperopic perception (Figure 4.9).....	45
Table 4.6 SSIM and PSNR table of hyperopic perception (Figure 4.10).....	46
Table 4.7 SSIM and PSNR table of the negative astigmatic perception	47
Table 4.8 SSIM and PSNR table of the positive astigmatic perception	48

CONTENTS

1 INTRODUCTION.....	17
1.1 Contributions.....	18
1.2 Thesis Structure	18
2 BACKGROUND.....	21
2.1 Sensation and Perception	21
2.2 Psychophysics	23
2.3 The Human Eye.....	24
2.3.1 Anatomy.....	24
2.3.2 Visual Aberrations	26
2.4 Optics and Wavefront Theory.....	28
2.5 Summary.....	29
3 RELATED WORK	31
3.1 Visual Simulation	31
3.1.1 Optical Simulation Techniques	31
3.1.2 Non-Optical Simulation Techniques	33
3.2 Estimating/Correcting Visual Optical Aberrations	33
4 VISUAL SIMULATION OF REFRACTIVE ERRORS	35
4.1 Target Images and Capture Setup.....	36
4.2 Modeling Visual Aberrations.....	37
4.3 Image Filtering	38
4.4 Validation.....	39
4.4.1 Vertex Distance and Ray Transfer Matrix.....	40
4.4.2 Comparison of Simulated Results with Ground Truth.....	43
4.5 Summary.....	55
5 ABSOLUTE THRESHOLD FOR VISION.....	57
5.1 Experimental Design.....	58
5.2 Participants.....	58
5.3 Quasi-Random Algorithm.....	59
5.4 Measurements	60
6 CONCLUSION	67
6.1 Future Work	68
REFERENCES.....	69
APPENDIX A — INDIVIDUAL PARTICIPANT DATA	73

1 INTRODUCTION

Vision is the primary channel we use to perceive the universe. Its unique capability allows us to acquire information about the surrounding world by sensing the intensity and color of light. This experience is unique and the perceived image is affected by several individual factors (*e.g.*, refractive errors, light sensitivity, distribution of photoreceptors in the retina, etc.). Simulating visual experience is a complex and difficult task, which requires the integration of a wide range of fields, including optics, anatomy, physiology, biochemistry, psychology, and cognitive neurosciences (SCHWARTZ, 2010).

Visual aberrations can be classified as low-order or high-order. Low-order aberrations (*i.e.*, myopia, hyperopia, astigmatism, and presbyopia) can be described in terms of spherocylindrical values and can be corrected with the use of eye glasses, contact lenses, or refractive surgery. They are responsible for about 90% of ones loss of visual acuity (DIAS-SANTOS et al., 2014). The remaining 10% is due to a combination of particular imperfections, known as high-order aberrations (*e.g.*, trefoil, coma, quadrafoil, secondary astigmatism). Visual aberrations can be described by the eye's point-spread function (PSF), often represented using the so-called wavefront maps. Figure 1.1 illustrates the human eye and the effects of some low-order aberrations when focusing at infinity.

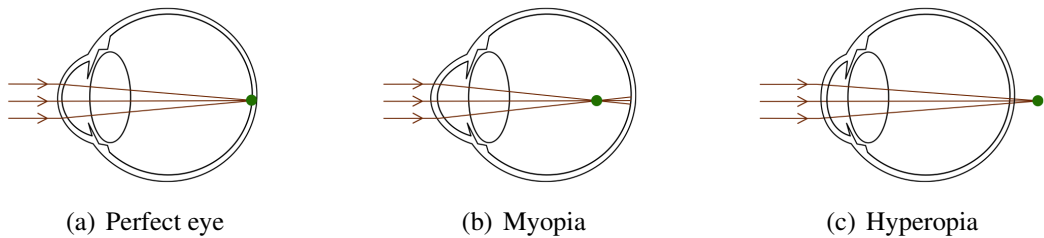


Figure 1.1 – The human eye and some low-order aberrations. (a) A perfect eye focuses the parallel rays to a single point on the retina; (b) a myopic eye has an elongated eye ball or a bumped cornea, focusing parallel rays at a point before the retina; (c) a hyperopic eye has a shallow eye ball or a flatter cornea, thus focusing parallel rays at point behind the retina (modified from (PAMPLONA et al., 2010)).

The simulation of how an impaired eye perceives a scene is a complex, but highly important task. It could, for instance, give doctors an idea of how a given patient's vision was before and after some surgical procedure. It could also allow primary school teachers understand the complaints of their students. In practice, poor visual performance is often misinterpreted as the perception of blurry images. However, the problem is not that simple. Visual simulation is an intricate process that requires sophisticated tools of Fourier analysis (THIBOS; THIBOS, 2011). From a simple geometrical perspective, when the optical system of an eye is mis-focused at a point in the scene, the light emitted/reflected by such a point is spread out across some area

(circle of confusion) of the retinal surface, causing blur. This can be understood from Figures 1.1(b) and 1.1(c), and observed in Figure 1.2(c), which was captured using a myopic camera. Note that when the optical system is well focused (Figure 1.1(a)) a point on the scene is imaged to a point on the retina.

Unlike traditional 2-D digital image processing in which an image is blurred by convolving it with a spatially-invariant low-pass filter kernel (Figure 1.2(b)), visual blurring is a depth-dependent phenomenon (*i.e.*, the amount of blurring introduced by the eye’s PSF varies with the distance from the observer’s focal plane to the scene element). If depth is not taken into account by the blurring method, the resulting image might be very different from the one formed onto the retina — Figure 1.2(c).

We present a practical approach to the problem of simulating how visual low-order aberrations affect the perception of monochromatic images. It relies on the assumption of a fixed depth and uses Fourier Tools and a DSLR camera to simulate and validate results.

1.1 Contributions

The main **contributions** of this thesis include:

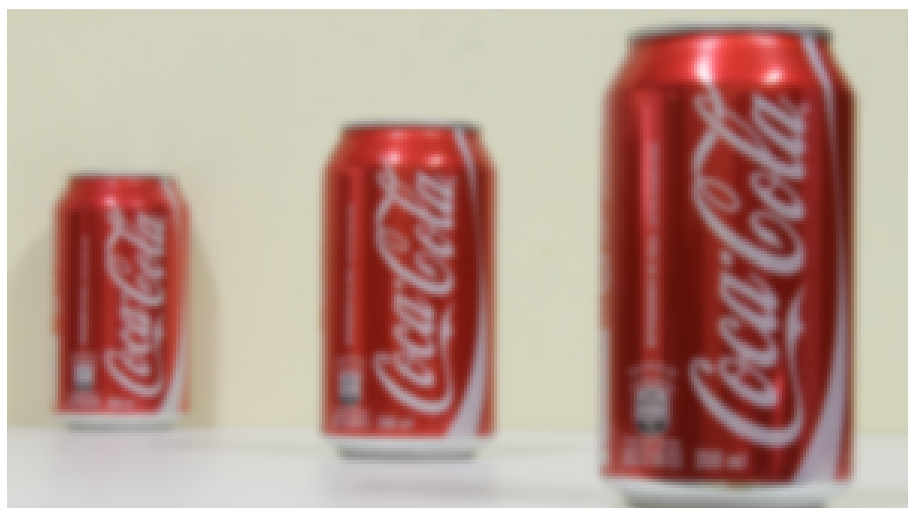
- A technique for modeling and simulating visual aberrations;
- A methodology to validate visual simulations’ outcomes;
- A psychophysical experiment about the visual absolute threshold.

1.2 Thesis Structure

The remaining of this thesis is organized as follows: Chapter 2 reviews the theoretical basis for the further anatomical, optical, and numerical discussions. Chapter 3 discusses previous visual simulation techniques, as well as methods for estimating optical aberrations. It also discusses simulation techniques that take non-optical characteristics into account. Chapter 4 presents our approach for visual simulation of blur on monochromatic images. Additionally, it explains how the technique can be combined with the minimum amount of light perceived by an individual. Chapter 5 presents our results. Finally, Chapter 6 summarizes this thesis and suggests some ideas for future work.



(a)



(b)



(c)

Figure 1.2 – A real scene with objects at different depths. (a) Photograph taken with a DSLR camera, with all objects in focus; (b) result of convolving the photograph in (a) with a 2-D low-pass filter. ($\sigma = 15$); (c) Adding an extra lens (+1 diopter) to the camera’s optical system to simulate myopia. Note how the amount of blurring increases with distance.

2 BACKGROUND

The study of how optical aberrations affect visual experience requires a more thorough understanding of human perception and the wave properties of light. In this chapter, we establish and review some of the theoretical principles that were used in the experimental studies, data analysis, interpretation of the results.

2.1 Sensation and Perception

Sensation and perception are the processes that put us in contact with stimuli from our world — objects and events (KING, 2012). Understanding these processes requires comprehending the physical properties of our perception and the study of the corresponding sensor, for example, light and the eye. Lemma (2005) defines some concepts that are necessary to explain how stimulation (*e.g.*, visual information) becomes meaningful perception: (i) *stimulus*: a source of physical energy that produces a response in a sense organ; (ii) *response*: any reaction of an organism to or in the presence of a stimulus; (iii) *transduction*: sequence of operations by which physical energy is transformed into patterns of neural impulses that give rise to sensory experience; (iv) *sensation*: process of receiving stimulus energies from external environment and transforming those energies into neural energy; and (v) *perception*: process whereby the brain interprets sensations, taking into account past experiences, the context in which the sensation occurs, and emotions.

The steps related to the perception of a visual information are illustrated in Figure 2.1, where light waves reflected from the butterfly act as stimuli to react with our sensory receptors, which convert the energy into neural signals. After that, neural messages travel to the sensory cortex of the brain and become sensations. Finally, the process of perception interprets these sensations and grant us to recognize a butterfly (ZIMBARDO; JOHNSON; MCCANN, 2012).

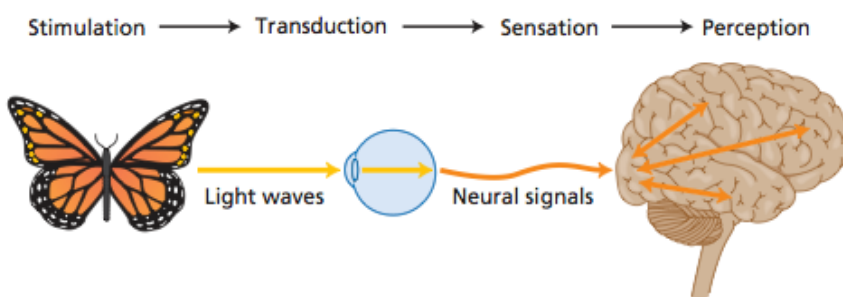


Figure 2.1 – General flow of sensory information from energy stimulus to sensory receptor cell to sensory neuron to sensation and perception (ZIMBARDO; JOHNSON; MCCANN, 2012).

Light is a form of electromagnetic (EM) radiation which travels through space in waves and can be described in terms of its physical characteristics — wavelengths and/or amplitude. Color and brightness are the psychological counterparts of light wavelength and intensity that exist only in the brain (KING, 2012). Humans are capable of detecting only a tiny segment of the EM spectrum, called visible light (Figure 2.2), which ranges in wavelength from approximately 400 to 700 nm ($1\text{nm} = 10^{-9}\text{m}$). Wavelengths outside this range are not detected by humans because they are not transmitted by the ocular media or cannot be absorbed by our retinal photopigments Schwartz (2010).

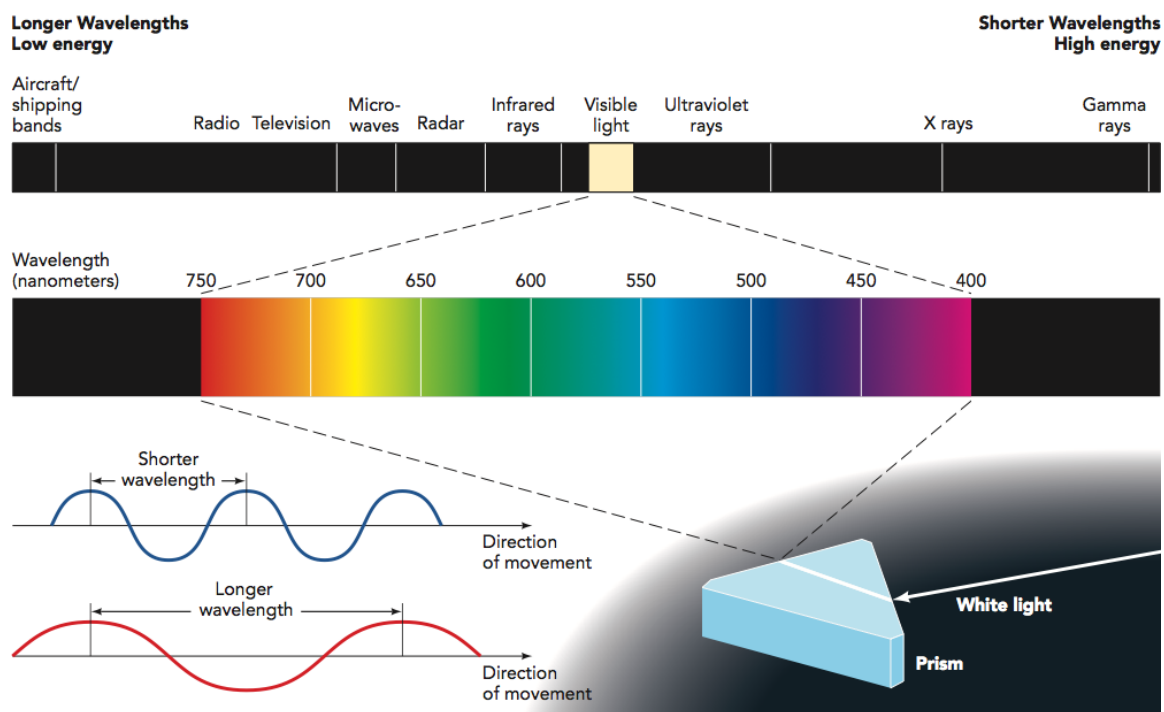


Figure 2.2 – The Electromagnetic Spectrum and Visible Light: (Top) Visible light is only a narrow band in the electromagnetic spectrum. Visible light wavelengths range from 400 to 700 nanometers. X rays are much shorter, radio waves much longer. (Bottom) The two graphs show how waves vary in length between successive peaks. Shorter wavelengths are higher in frequency, as reflected in blue colors; longer wavelengths are lower in frequency, as reflected in red colors (KING, 2012).

Distinct neural messages flows into the nervous system as information, and it's type depends on the energy captured by a sensory receptor. Figure 2.3 shows the human sensory receptors for vision, hearing, touch, smell, and taste. In order to generate a sensory experience from any receptor, there is a minimal amount of physical energy needed - known as absolute threshold (ZIMBARDO; JOHNSON; MCCANN, 2012).

Table 2.1 shows some typical absolute threshold levels for several familiar stimuli. Experiments designed to determine thresholds, and the study of the relationship between physical nature of stimuli and people's response to them belong to a branch of psychology called *psychophysics* (LEMMA, 2005).

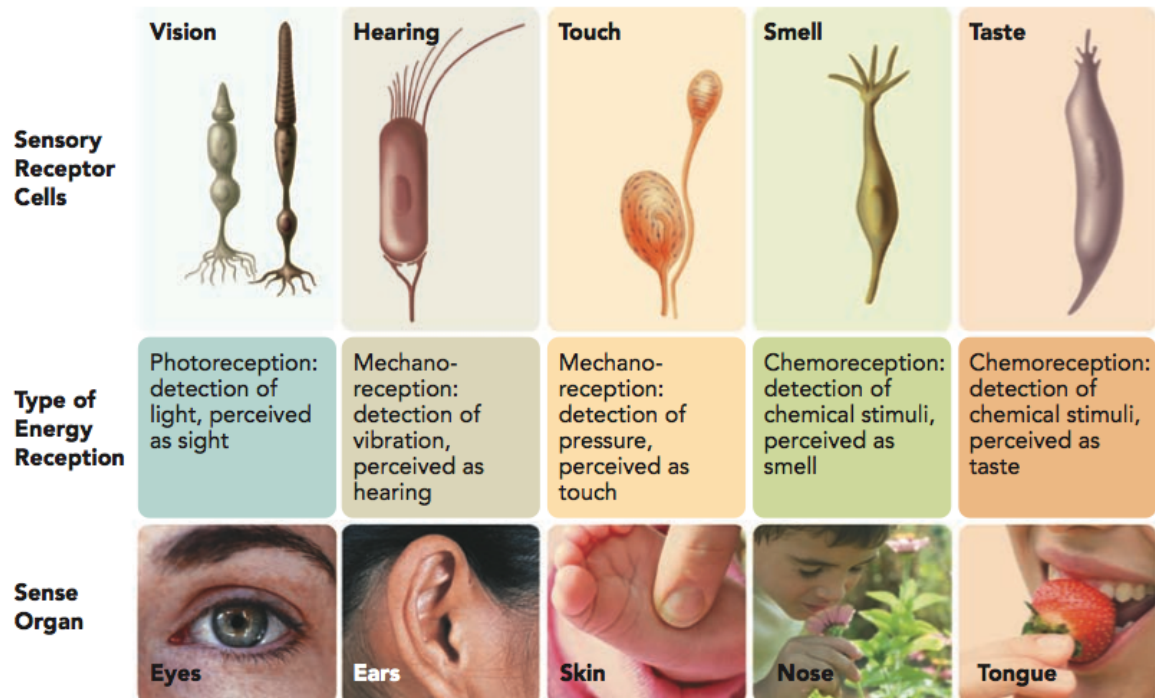


Figure 2.3 – Human Senses: organs, energy stimuli, and sensory receptors (KING, 2012).

Table 2.1 – Sensory threshold of five senses (ZIMBARDO; JOHNSON; MCCANN, 2012).

Sense	Detection Threshold
Sight	A candle flame at 30 miles on a clear, dark night
Hearing	The tick of a watch 20 feet away in a quiet room
Smell	One drop of perfume diffused throughout a three-room apartment
Taste	One teaspoon of sugar in 2 gallons of water
Touch	A bee's wing falling on the cheek from 1 centimeter above

2.2 Psychophysics

The term *psychophysics* was invented in 1860 by Gustav Theodor Fechner, a German physicist and philosopher, as a mathematical approach to relate mental and physical events on the basis of experimental data (TREUTWEIN, 1995). Generally, all sensory systems are able to detect varying degrees of energy, and psychophysical experiments frequently involve the determination of some absolute threshold. This is a complicated task because humans are not perfect observers. Lemma (2005) emphasizes that the thresholds determined by experiments or clinical procedures may be influenced by several factors, including decision criteria, attention, motivation, and internal neural noise. Further details about Fechner's original methods for determining absolute thresholds and some recent improvements are discussed in (KLEIN, 2001; LEEK, 2001; BLAKE; SEKULER, 2005).

2.3 The Human Eye

The eye is a sophisticated imaging system capable of dynamically adjusting its refractive power to focus at a wide range of depths. Optical aberrations in this imaging system are the main causes of loss of visual acuity. *Visual acuity* (*i.e.*, the eye's ability to see fine details) can be determined with an auxiliary chart, in which the individual must resolve its details (*e.g.*, bars and gaps) to recognize targets, such as Snellen or Sloan letters (Figure 2.4). The ability to distinguish between two details determines the *Minimum Angle of Resolution* (MAR). The standard visual acuity for humans is 1 arc minute (one-sixtieth of one degree) (SCHWARTZ, 2010). In ophthalmology, visual acuity is commonly recorded in the form of the *Snellen fraction*: $VA = D'/D$, where D' is the standard viewing distance (usually 20 feet) and D is the distance at which each letter in the chart line subtends 5 arc minutes. The larger the D value, the worse the vision. The term 20/20 vision is the standard for emmetropes (*i.e.*, at a 20 feet distance, a person with normal vision should be able to read the small 20/20 line on an eye chart).

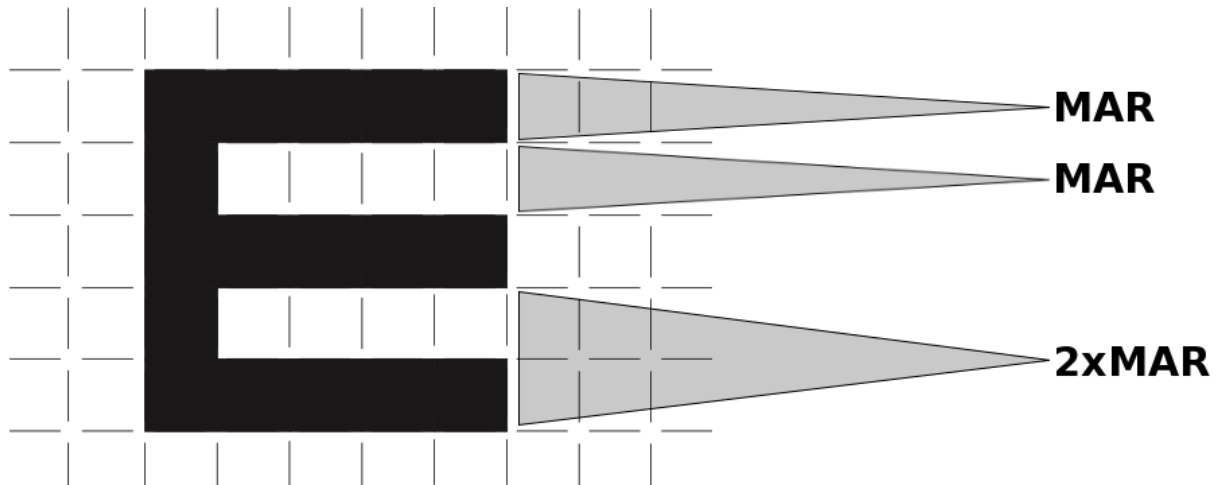


Figure 2.4 – Construction of the optotype E. The detail (a bar or a gap) is one-fifth of the overall size of the optotype. MAR stands for Minimum Angle of Resolution, which corresponds to 1 arc minute. Modified from Schwartz (2010).

2.3.1 Anatomy

The human eye is constituted of several tissues, which contains approximately 126 million receptors cells (KING, 2012). It can be divided into three concentric layers and two chambers, plus the iris, pupil, and lens. In an adult, it has an average length of 25.4 mm. The

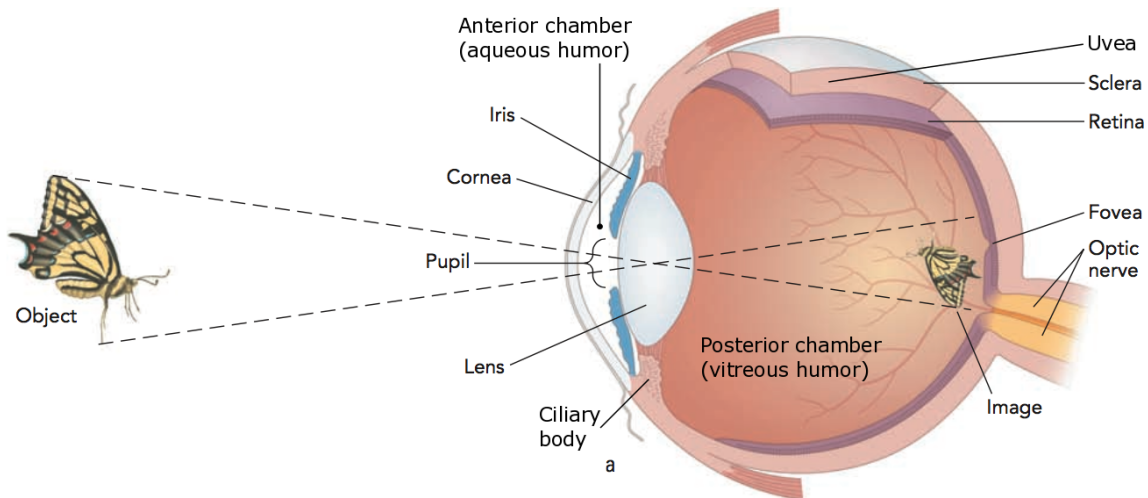


Figure 2.5 – Parts of the Eye. Note that the image of the butterfly on the retina is upside down. The brain allows us to see the image right side up. (modified from King (2012)).

outermost layer is the *sclera*, the middle layer is the *uvea*, and the innermost layer is the *retina*.

Figure 2.5 shows a cross section an a human eye and its parts.

The sclera averages about 1 millimeter in thickness and is made of tightly packed, interwoven fibers that guarantee its toughness. The sclera needs to be tough due to eyeball's pressure, which is the double of the atmospheric pressure (BLAKE; SEKULER, 2005). There is a transparent membrane at the very front of the eye, called *cornea*. The cornea is responsible for two-thirds (40 diopters) of the eye's refractive power (total power of 60 diopters) (TKACZYK, 2010). Most part of the uvea layer consists of a heavily pigmented, spongy structure called the *choroid*. The choroid averages 0.2 mm thick and contains a network of blood vessels, including capillaries, for blood supply. Its pigmentation reduces light scattering by capturing light that is not captured by the retinal receptor cells. According to King (2012), the "retina is a light-sensitive surface that records electromagnetic energy and converts it to neural impulses for later processing". It has two kinds of photoreceptors (*i.e.*, light sensitive receptors cells): rods and cones. The retina resembles a very thin, fragile meshwork, which explains its name — *rete* is Latin for "fisherman's net" (BLAKE; SEKULER, 2005).

Both anterior and posterior chambers contains a specific humor (Figure 2.5), which is a transparent liquid continuously produced by the ciliary body. Both aqueous and vitreous humors serve a number of important functions, as maintain the eyeball's shape and nourishment. The iris is the circular section of tissue that gives the eye its characteristic color: brown, blue, green, etc. In the middle of the iris there is the pupil, whose size varies according to the illumination level with the help of two sets of muscles — the inner and radial (SCHWIEGERLING, 2004). Its average diameter varies from 2 millimeters to 8 millimeters, and depends on several factors,

such as individual characteristics and luminance level (YODER; VUKOBRATOVICH, 2011).

Right behind the iris, lies an important optical element of the eye, the crystalline lens (see Figure 2.5). A gradient-refractive-index lens that contributes approximately one-third (20 diopters) of the dioptric power of the eye, and modifies its shape to focus on near or distant objects (SCHWIEGERLING, 2004). This variation, from nearly flat to rounder, causes changes in the final optical power and is called *accommodation*. Through accommodation, the lens can correctly focus on the retina the light coming from the scene. For good vision, the crystalline lens must be transparent. Loss of transparency, known as *cataracts* leads to a decrease in vision quality (SCHWARTZ, 2010).

2.3.2 Visual Aberrations

Visual aberrations are the main cause of visual impairment. Estimates indicate that there are about 153 million people with visual impairment due to uncorrected refractive errors (WHO, 2007). Thibos et al. (2002) defined standards for reporting of optical imperfections of eyes. The method of choice for assessing eye aberrations (*i.e.*, describing its wavefront aberration) are the so called *Zernike polynomials*. They consist of a series of orthogonal polynomials over the area of a unitary circle (Figure 2.6) and can be expressed either in Cartesian (X, Y) or polar (θ, ρ) coordinate systems. The conversions between the two are given by:

$$\begin{aligned} \rho &= \sqrt{x^2 + y^2} & \theta &= \tan^{-1}(y/x) \\ x &= \rho * \cos \theta & y &= \rho * \sin \theta \end{aligned} \quad (2.1)$$

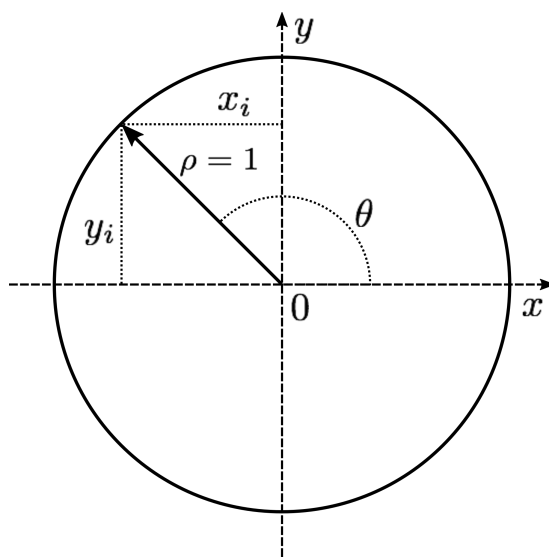


Figure 2.6 – The unit circle.

There are several different normalization and numbering schemes for representing Zernike polynomials. Here we adopt a double indexing scheme (Z_n^m , where n is the *order* and m is the *frequency* – see Figure 2.7). Such a scheme is defined as:

$$Z_n^m(\rho, \theta) = \begin{cases} N_n^m R_n^{|m|}(\rho) \cos m\theta, & \text{for } m \geq 0, \\ -N_n^m R_n^{|m|}(\rho) \sin m\theta, & \text{for } m < 0, \end{cases}$$

where N_n^m , $R_n^{|m|}$ and the sinusoidal functions stand for the normalization factor, radial component, and azimuthal component, respectively. Such terms are fully described by Thibos et al. (2002). Some of the *Zernike polynomials* (up to the 5th order) are listed in Table 2.2 and illustrated in Figure 2.7. They can be applied directly to wavefront evaluation in the eye's pupil. In ophthalmology, the radial degree n is the basis for classifying aberrations as lower-order ($n \leq 2$) and higher-order ($n > 2$). However, the vertical and horizontal tilt, as well the zeroth-order piston polynomial, are not considered in measurements of image focus quality (MEISTER, 2010).

Table 2.2 – Zernike polynomials up to the fifth order.

j	n	m	Zernike Polynomials	Name
0	0	0	1	piston
1	1	-1	$2\rho \sin \theta$	vertical tilt
2	1	1	$2\rho \cos \theta$	horizontal tilt
3	2	-2	$\sqrt{6}\rho^2 \sin \theta$	oblique astigmatism
4	2	0	$\sqrt{3}(2\rho^2 - 1)$	defocus
5	2	2	$\sqrt{6}\rho^2 \cos \theta$	vertical astigmatism
6	3	-3	$\sqrt{8}\rho^3 \sin 3\theta$	vertical trefoil
7	3	-1	$\sqrt{8}(3\rho^3 - 2\rho) \sin \theta$	vertical coma
8	3	1	$\sqrt{8}(3\rho^3 - 2\rho) \cos \theta$	horizontal coma
9	3	3	$\sqrt{8}\rho^3 \cos 3\theta$	oblique trefoil
10	4	-4	$\sqrt{10}\rho^4 \sin 4\theta$	oblique quadrafoil
11	4	-2	$\sqrt{10}(4\rho^4 - 3\rho^2) \sin 2\theta$	oblique secondary astigmatism
12	4	0	$\sqrt{5}(6\rho^4 - 6\rho^2 + 1)$	primary spherical
13	4	2	$\sqrt{10}(4\rho^4 - 3\rho^2) \cos 2\theta$	vertical secondary astigmatism
14	4	4	$\sqrt{10}\rho^4 \cos 4\theta$	vertical quadrafoil
15	5	-5	$\sqrt{12}\rho^5 \sin 5\theta$	vertical pentafoil
16	5	-3	$\sqrt{12}(5\rho^5 - 4\rho^3) \sin 3\theta$	vertical secondary trefoil
17	5	-1	$\sqrt{12}(10\rho^5 - 12\rho^3 + 3\rho) \sin \theta$	vertical secondary coma
18	5	1	$\sqrt{12}(10\rho^5 - 12\rho^3 + 3\rho) \cos \theta$	horizontal secondary coma
19	5	3	$\sqrt{12}(5\rho^5 - 4\rho^3) \cos 3\theta$	oblique secondary trefoil
20	5	5	$\sqrt{12}\rho^5 \cos 5\theta$	oblique pentafoil

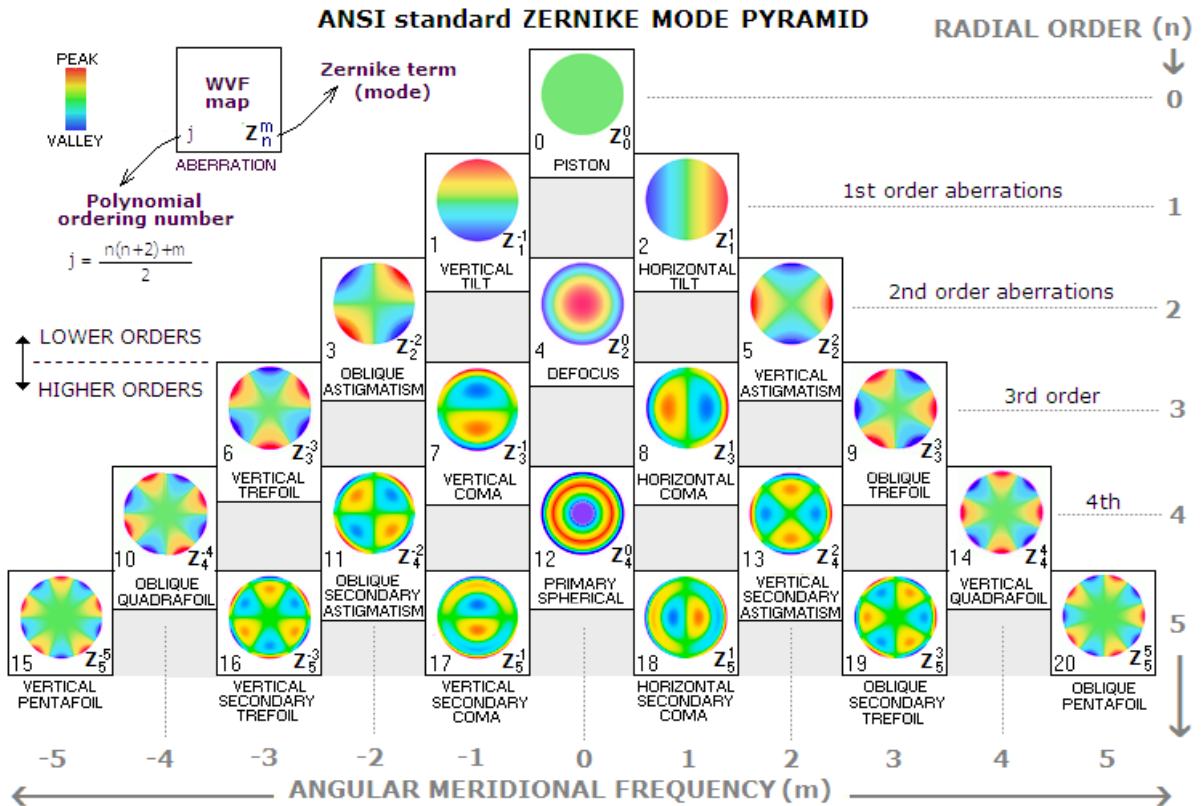


Figure 2.7 – The Zernike expansion pyramid: a function of term's radial degree (or order) n and azimuthal frequency m (SACEK, 2015).

2.4 Optics and Wavefront Theory

The human eye consists of several optical components, notably the cornea, the crystalline lens, the pupil, and the retina. Visual aberrations are the combination of the imperfections/anomalies from the outermost to the innermost component. The aim of vision correction is to remove or to minimize the ocular aberrations of the visual system. But to achieve this goal, we first need to understand and analyze how light behaves inside the eye.

According to Sacek (2015) even though *geometrical optics* provides a proper way of determining image location and magnification by tracking paraxial rays, the determination of optical systems' aberrations require more complex calculation considering light waves and its propagation (*i.e., physical optics*).

Dai (2008) states that "a propagating wavefront can be characterized as many rays propagating in different directions as determined by the local slopes of the wavefront surface". Suppose there is an original wavefront $W(x, y)$, centered at point O and conformed within the aperture Σ , as shown in Figure 2.8(a). When it propagates towards an eye by a distance d , it becomes

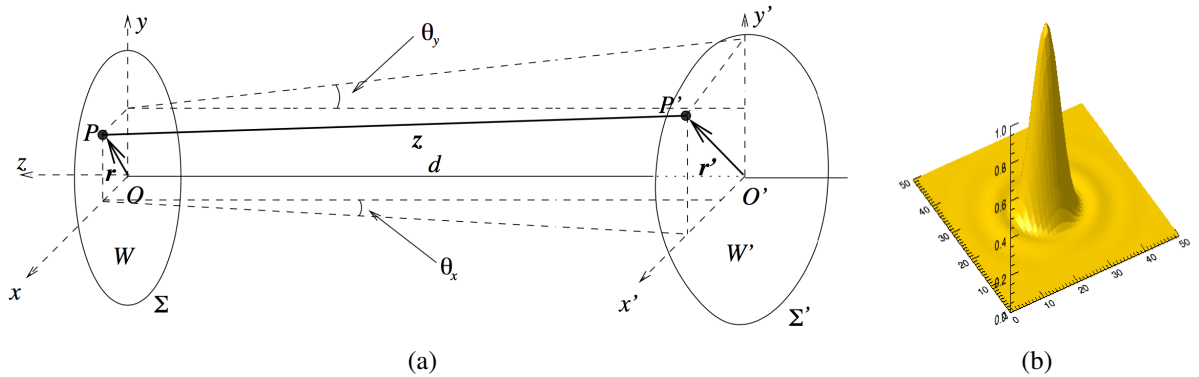


Figure 2.8 – General concepts of wavefront: (a) Geometry of the wavefront propagation (DAI, 2008); (b) the PSF generated by an aberrated wavefront (SMITH, 2015).

a new wavefront $W'(x', y')$ given as

$$W'(x', y') = W(x, y) + z(x, y; x', y'), \quad (2.3)$$

where $z(x, y; x', y')$ is the distance between points $P(x, y)$ and $P'(x', y')$ (Figure 2.8(a)), and can be written as:

$$z(x, y; x', y') = \sqrt{d^2 + (x - x')^2 + (y - y')^2}. \quad (2.4)$$

The propagation of a wavefront $W(x, y)$ consisting of low-order aberrations only, expressed with Zernike Polynomials, is discussed by (DAI, 2008). In addition, the author discusses several optical metrics of ocular wavefronts. A very good predictor for visual performance is the point spread function (PSF), which describes how a ray of light is dispersed in a given space. It is represented by a 2-D array and, as shown in Figure 2.8(b), resembles a surface in 3-D. It can be obtained using Fourier Optics (GOODMAN, 2005) and the eye's wavefront aberration information.

2.5 Summary

This chapter reviewed the background information about the human eye required for understanding the remaining of this thesis.

3 RELATED WORK

Vision simulation has been addressed in different ways over the years. Since the first synthetic image with depth of field computed by Potmesil and Chakravarty (1981), there has been a significant number of computer graphics techniques addressing the rendering of realistic effects. More recently, the possibility of estimating and compensating for refractive errors has attracted the attention of several researchers, mainly addressing the formulation of interactive, portable, and inexpensive solutions. The following subsections describe the main techniques for simulating, estimating, and correcting visual aberrations.

3.1 Visual Simulation

3.1.1 Optical Simulation Techniques

Barsky (2004) proposed a method for generating synthetic images incorporating the optical characteristics of an individual. Specifically, his method simulates the perception of an individual based on data acquired using a Shack-Hartmann wavefront aberrometer. Figure 3.1 shows a rendered image using his technique, along with an overview of the algorithm. Note that once the wavefront data is captured, it is sampled to calculate an *Object Space PSF* (OSPSF) and used to blur the input synthetic scene at different depths.

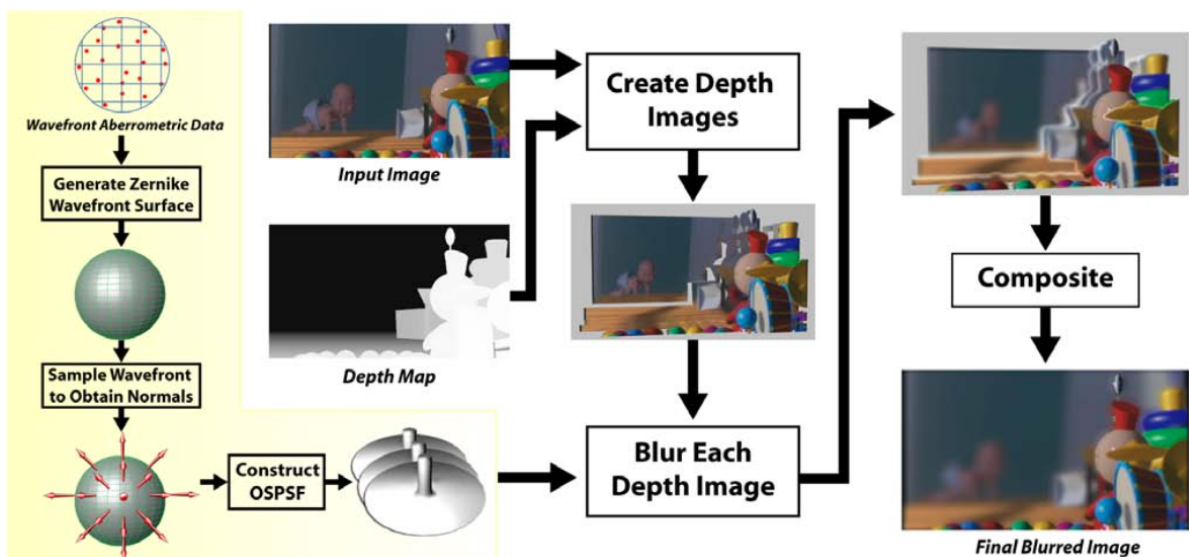
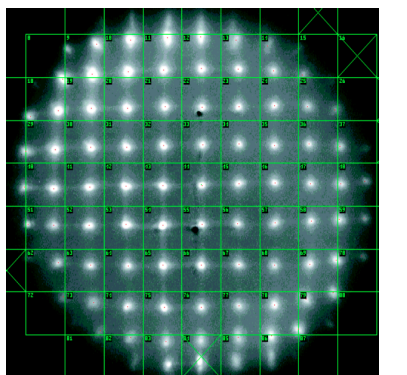


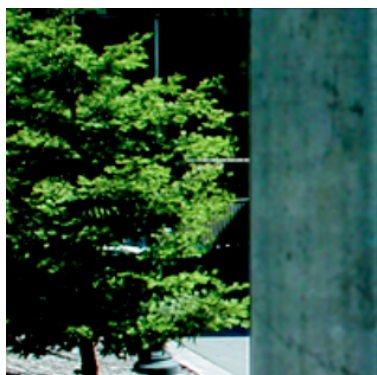
Figure 3.1 – Overview of the vision-realistic rendering algorithm proposed by Barsky (2004). Given an individual's wavefront data and some synthetic scene, one can generate millions of samples necessary to calculate an OSPSF; create a set of depth images; blur each depth image; and composite them to obtain a final blurred image.

Many researchers have used raytracing techniques and anatomical optics to study and simulate vision by using theoretical models of the human eye (CAMP; MAGUIRE; ROBB, 1990; KOLB; MITCHELL; HANRAHAN, 1995). Camp, Maguire and Robb (1990) described two ray tracing algorithms for deriving an optical PSF from corneal topography measurements. They focused on simulating and evaluating optical performance of patients' eyes with the following corneal pathologies: *keratoconus*, *epikeratophakia for aphakia* and *radial keratotomy*. Kolb, Mitchell and Hanrahan (1995) presented a physically-based camera model that simulates aberration and radiation. To simulate such effects, they compute the geometry of image formation of a particular lens system using a modified distributed ray tracing algorithm. The algorithm is a hybrid of rendering and lens maker techniques, and can produce images of synthetic scenes showing a variety of optical effects. Mostafawy, Kermani and Lubatschowski (1997) combined the algorithm presented by Kolb, Mitchell and Hanrahan (1995) and the dimensions of an schematic eye model to generate virtual simulations of vision after corrective surgery.

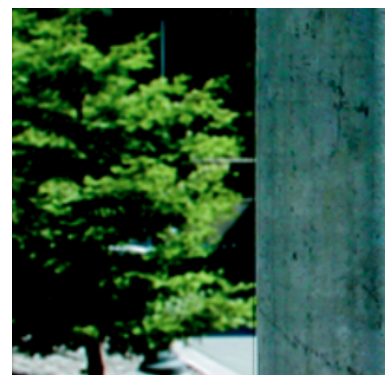
Moreover, the study of monochromatic aberrations of the human eye with wavefront sensors (LIANG et al., 1994) allowed many others to perform simulations by using Fourier tools to mimic visual perception. Yu (2001) presents a technique capable of generating simulations of synthetic and real scenes focusing at a specific depth (Figures 3.2(b) and 3.2(c)). Instead of considering only the corneal surface and using raytracing techniques to perform such simulations, the authors rely on data captured by a Shack-Hartmann device (Figure 3.2(a)). With this information they construct a wavefront, which is used to blur a sharp image according to a depth map. However, they do not present a proper way of evaluating the simulations' outcomes, which could be, for example, compared with an optical ground truth. Watson and Ahumada Jr (2008) proposed an image-based model for predicting acuity from optical aberrations. In this model, a 'neural image' is computed incorporating optical and neural filtering. Then, this image



(a) Shack-Hartmann device's output



(b) Focused at infinity



(c) Focused at 0.5m

Figure 3.2 – Yu (2001) uses data captured using a Shack-Hartmann aberrometer (a) to simulate blur at specific depth values (b) and (c).

is presented to four human observers and the LogMAR acuity is evaluated. By doing this, they can relate visual acuity as a function of a particular aberration and compute predictions of how a specific aberration (*e.g.*, defocus) affects visual acuity.

3.1.2 Non-Optical Simulation Techniques

Some techniques are concerned with modeling the effects caused by non-optical issues and use them to achieve more realistic synthetic images. One example is the method proposed by Deering (2005). His approach describes a retinal photon-accurate model of the human eye. Such a model is used together with computer graphics techniques and a simplified eye's optical model to produce synthetic simulations of the image formation process.

Another technique that explores different effects caused by the anatomy of the human eye — the glare — is discussed by Ritschel et al. (2009). The authors proposed a model for a real-time dynamic simulation of the scattering in the human eye (Figure 3.3), which is efficiently implemented by drawing a few basic primitives, applying an FFT, and doing a special kind of blur. They have also performed psychophysical studies to measure the perception of brightness for glare models. However, they state that, as any other intrinsic phenomena, no ground truth can be obtained. And the model's validation remains a challenging task.

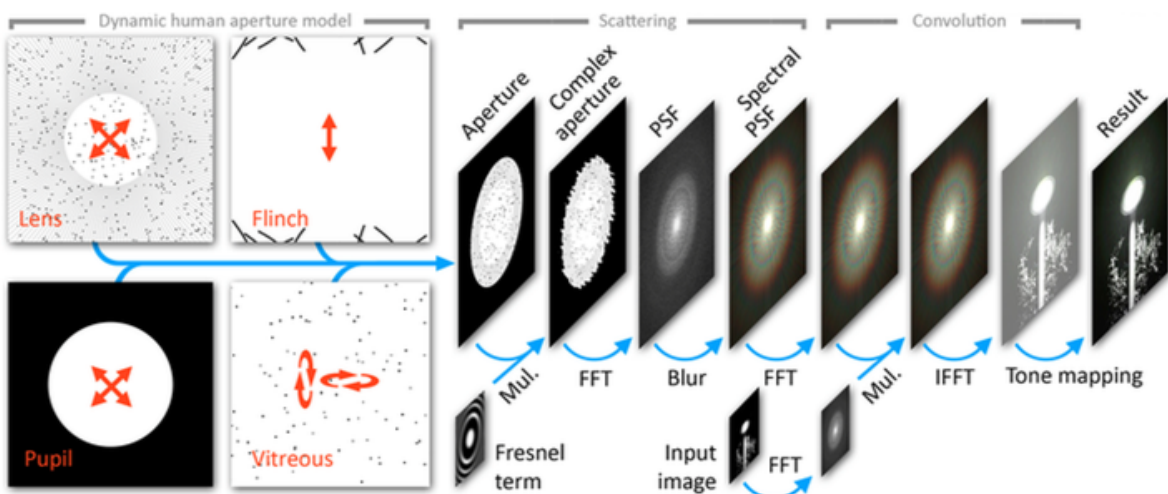


Figure 3.3 – The temporal glare pipeline (RITSCHEL et al., 2009).

3.2 Estimating/Correcting Visual Optical Aberrations

Pamplona et al. (2010) presented a practical approach for estimating low-order aberrations without the need of expensive equipments. It uses a pinhole mask attached to a smartphone displaying patterns to the subject. The aberrations are estimated by the subjective alignment of the different patterns. Kronbauer et al. (2011) developed a psychophysical approach for vision measurement in candelas. It consists in presenting light stimulus in a display in order to discover the absolute threshold for clear and dark conditions. Then, by relating it with an objective vision's assessment (*e.g.*, vision chart acuity and aberrometry data), they have stated a strong correlation between aberrometry data and the absolute threshold.

Many methods have achieved the goal of free the viewer from needing wearable optical correction when looking at displays (HUANG et al., 2012; PAMPLONA et al., 2012; HUANG et al., 2014), and printings or projections (MONTALTO et al., 2015). Other works have explored physiologically-based models to provide insights and feedback on how to produce high-fidelity effects and improve visualization experiences (MACHADO; OLIVEIRA; FERNANDES, 2009; PAMPLONA; OLIVEIRA; BARANOSKI, 2009; PAMPLONA et al., 2011).

4 VISUAL SIMULATION OF REFRACTIVE ERRORS

This chapter describes the approach used for visual simulation of low-order refractive errors. Figure 4.1 illustrates its pipeline, showing equivalent operations specified both in the spatial and in the frequency domain. Since we are primarily interested in visual acuity, all experiments and discussions presented here are based on monochromatic images. As visual blurring is a depth-dependent phenomenon, we have adopted the simplifying assumption that the observed images are at some constant depth. For this, we used two sets of charts containing standard Sloan letters (Figure 4.2): black letters on white background, as well as white letters on black background. The following sections provide the details of each step.

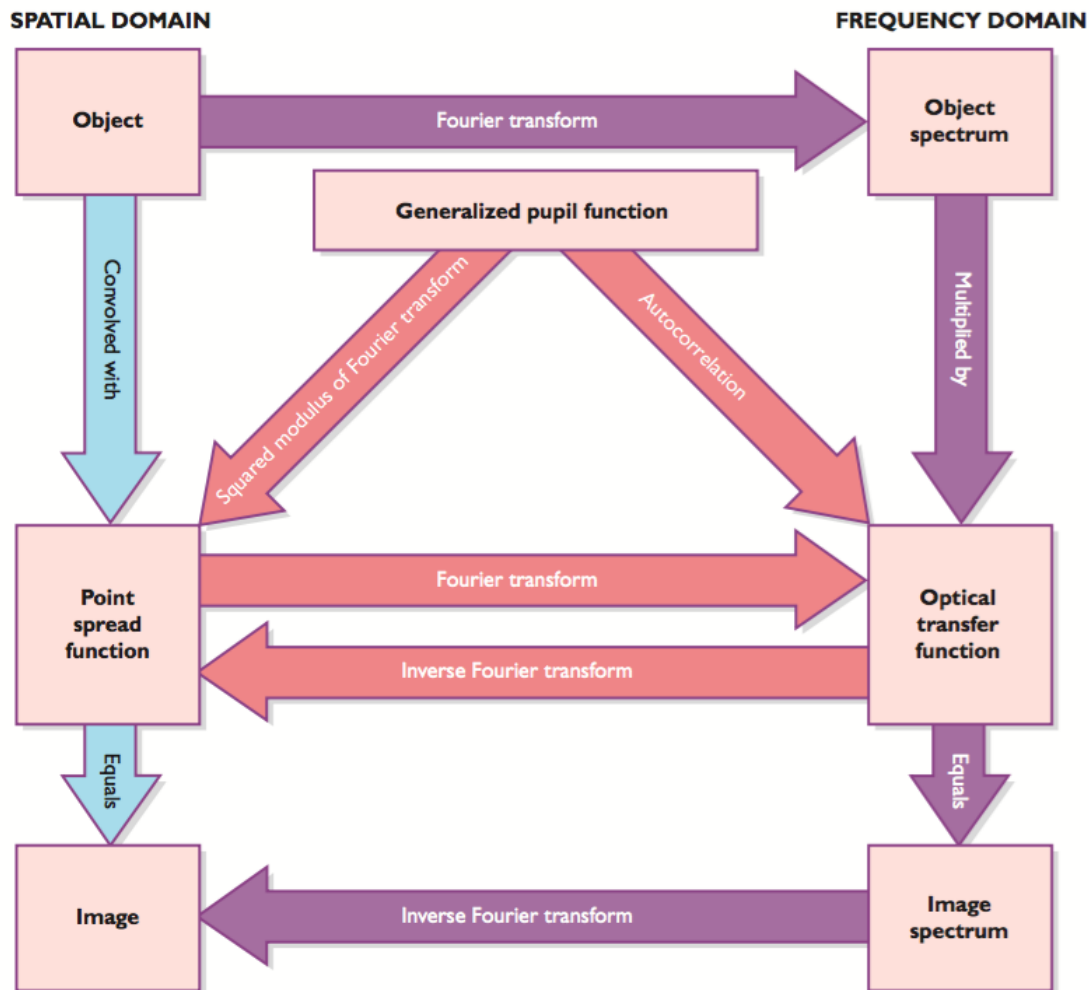


Figure 4.1 – The pipeline for simulating visual aberrations. In the spatial domain one needs the eye's point spread function (PSF), whereas in frequency domain the optical transfer function (OTF) is required (MOLLON, 2003).

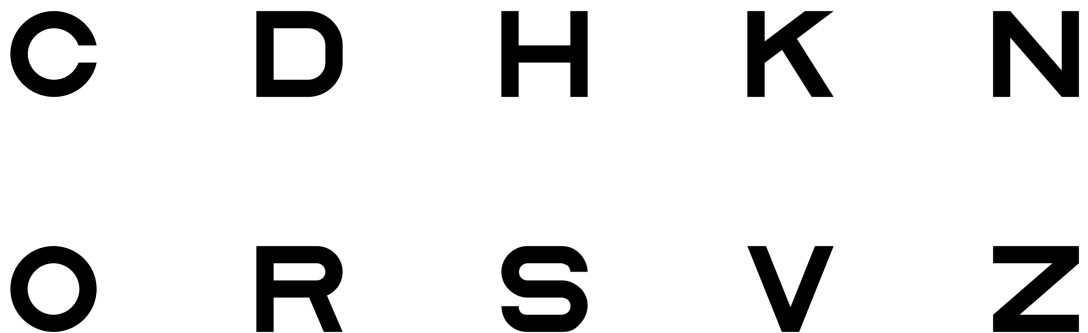


Figure 4.2 – Standard Sloan Letters.

4.1 Target Images and Capture Setup

We have created images of Sloan letters with values ranging from -0.3 to 1.0 in steps of 0.1 in the LogMAR (Logarithm of the Minimum Angle of Resolution) scale (BAILEY; LOVIE, 1976). Such an interval corresponds to the range from 20/10 to 20/200, respectively, in the Snellen scale. The LogMAR scale provides a more accurate estimate of visual acuity when compared to other charts (*e.g.*, Snellen), being the recommended one for research settings. Our target images were created according to Equation 4.1 for testing vision from three feet away. The individual letters were rendered using the vector graphics capabilities of Inkscape and the Sloan PostScript fonts provided by Pelli, Robson et al. (1988) (Figure 4.2). At the prescribed distance, the ratio between one pixel and one arc minute is 1:1, that is, the letters with a LogMAR value of 0 (or Snellen fraction 20/20) has exactly 5 pixels of height. For the purpose of our simulations, each black (white) letter (also called an *optotype*) was placed against a 113×133 -pixel black (white) square. Since $1 \text{ degree} = 60 \text{ arc minutes}$, each such square covers a total field of view (FOV) of $1,88^\circ \times 1,88^\circ$. The conversion from *Snellen decimal acuity* values to LogMAR values is presented in Equation 4.2. A Snellen decimal acuity value is the decimal representation of the equivalent Snellen ratio (*e.g.*, Snellen ratios of 20/20 and 20/40 correspond to Snellen decimal acuity values of 1.0 and 0.5, respectively).

$$\text{letter size}_{mm} = \left\{ \tan \left[\text{deg2rad} \left(\frac{5}{60} \right) \right] \times (\text{chart distance}_{mm}) \times (10^{-\text{LogMAR}})^{-1} \right\} \quad (4.1)$$

$$\text{LogMAR} = -\log_{10}(\text{Snellen decimal acuity}) \quad (4.2)$$

We have prepared white- and black-background LogMAR charts containing Sloan letters specifically designed for a viewing distance of three feet (Figure 4.3). The charts were printed at 360 dpi on white paper using a laser printer. We then took pictures of the charts with a DSLR camera. The camera was placed at three feet (91.44 cm) from the chart, with focal length set to 18mm. Since images acquired using this setup respect the 1:1 ratio between pixels and arc minutes, one can crop the squares containing the individual optotypes for further processing.

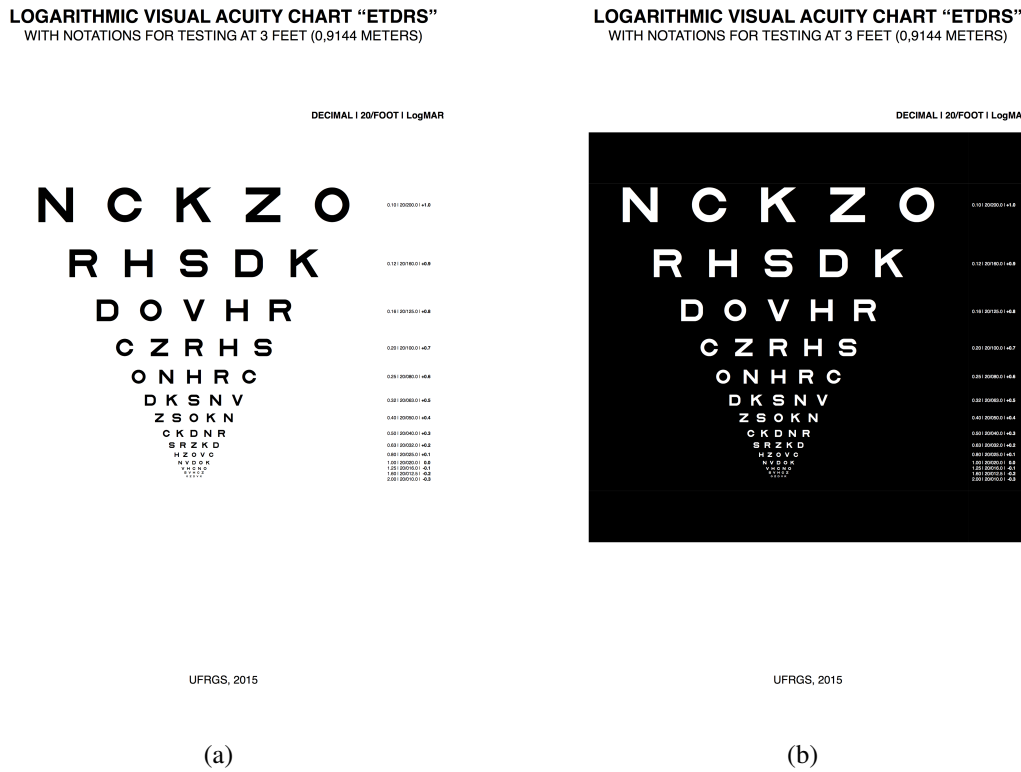


Figure 4.3 – LogMAR charts printed at 360 dpi on white paper using a laser printer. (a) Black letters on white background and (b) white letters on black background. The top row of each table corresponds to Snellen 20/200 (LogMAR +1.0) visual acuity when viewed from three feet. The bottom row corresponds to Snellen 20/10 (LogMAR -0.3) visual acuity when viewed from three feet away.

4.2 Modeling Visual Aberrations

We characterize the optical aberrations of the human eye using a wavefront aberration function. Such a function defines a wavefront map, which is approximated using a series of polynomials, such as the Zernike polynomials (see Section 2.3.2). Obtaining a complete wavefront function, which models both low-order and high-order aberrations, requires access to expensive wavefront aberrometer devices. In this work, we only consider the low-order aberrations (*i.e.*, myopia, hyperopia, and astigmatism), which can be easily obtained from any eyeglass

or contact lens prescription. One should note, however, that low-order aberrations are responsible for about 90% of one's total visual aberrations (DIAS-SANTOS et al., 2014). This should not come as a surprise, given that eyeglasses only correct for low-order aberrations and are the primary way of achieving corrected 20/20 vision. We obtain wavefront aberration function $W_{(x,y)}$ from prescription data as (DAI, 2008):

$$W_{(x,y)} = \sum_{i=-1}^1 c_2^{2i} Z_2^{2i}{}_{(x,y)}, \quad (4.3)$$

where

$$c_2^{-2} = \frac{R^2 * C * \sin(2\phi)}{4\sqrt{6}}, \quad (4.4)$$

$$c_2^0 = -\frac{R^2 * (S + C/2)}{4\sqrt{3}}, \quad (4.5)$$

$$c_2^2 = \frac{R^2 * C * \cos(2\phi)}{4\sqrt{6}} \quad (4.6)$$

and c_2^{-2} , c_2^0 , and c_2^2 are the coefficients of the Zernike polynomials corresponding to *oblique astigmatism* (Z_2^{-2}), *defocus* (Z_2^0), and *vertical astigmatism* (Z_2^2), respectively (see Figure 2.7). S , and C are respectively the *sphere* and *cylinder* values that specify the optical power in diopters (D). ϕ is cylinder axis expressed in degrees. The values S , C , and ϕ are popularly referred to as the "degree", the "astigmatism", and the "axis of astigmatism" in one's prescription. R is the radius of the subject's pupil (an aperture, in general) measured in mm, and c_2^{-2} , c_2^0 and c_2^2 are in μm . Figure 4.4 illustrates a wavefront map obtained for $S = 0.5\text{D}$, $C = -2.0\text{D}$, $\phi = 45^\circ$, and $R = 1.5\text{mm}$. If no aberration is present, the resulting wavefront is planar.

4.3 Image Filtering

Given S , C , R , and ϕ , one can obtain the effective aberration function as $kW_{(x,y)}$, where k is the spherical wavenumber (*i.e.*, $k = 2\pi/\lambda$), and $W_{(x,y)}$ is the wavefront aberration function expressed using the Zernike polynomials. For the case of low-order aberrations, $W_{(x,y)}$ is defined by Equation 4.3, which takes into account oblique astigmatism, defocus, and vertical astigmatism. $\lambda = 550\text{nm}$ is a standard wavelength used for monochromatic simulation (DAI, 2008). The pupil function $P_{(x,y)}$ is a binary function that evaluates to 1 inside the projected aperture, and 0 outside it. According to Goodman (2005), the *generalized pupil function* $\mathbb{P}_{(x,y)}$ is given

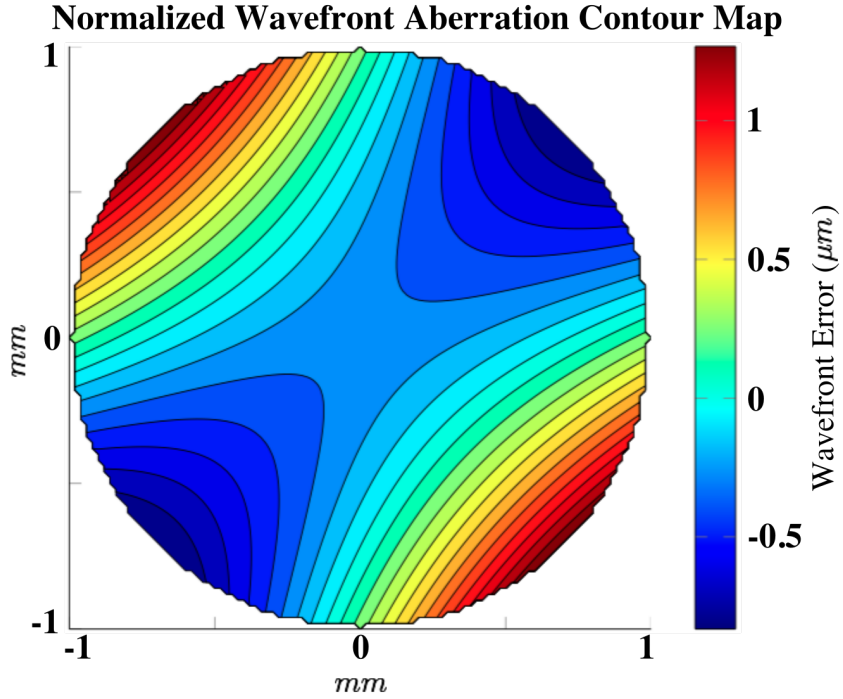


Figure 4.4 – Normalized wavefront map for an eye with: $S = 0.5\text{D}$, $C = -2.0\text{D}$, $\phi = 45^\circ$ and $R = 1.5\text{mm}$. The map represents a pupil with a radius of 1.0mm. The wavefront error (in μm) is the deviation of the wavefront aberration function $W_{(x,y)}$ (Equation 4.3) from a plane wave.

by:

$$\mathbb{P}_{(x,y)} = P_{(x,y)} \exp[j * k * W_{(x,y)}], \quad (4.7)$$

where $j = \sqrt{-1}$. Note that $\mathbb{P}_{(x,y)}$ is a complex number. One can obtain the point spread function of the optical system as the power spectrum of \mathbb{P} , *i.e.*, $\text{PSF} = |\mathcal{F}(\mathbb{P})|^2$, where \mathcal{F} is the Fourier transform operator. Given the PSF and an input image I , one can simulate the view of I through the given optical system computing the 2-D convolution $O = \text{PSF} \otimes I$. A more efficient computation of O can be obtained in the frequency domain (this is illustrated by purple arrows in Figure 4.1). In that case, $O = \mathcal{F}^{-1}(\mathcal{F}(I) * \text{OTF})$, where $\text{OTF} = \mathcal{F}(\text{PSF})$ is the *the optical transfer function* and $*$ is the element-wise multiplication.

4.4 Validation

To validate the visual simulation results of the refractive errors, we use a DSLR camera (Canon model EOS Rebel T3 with an 18-55mm zoom lens). The camera represents a perfect eye (*i.e.* without refractive aberrations). We place additional lenses in front of the camera's optical system to induce low-order aberrations (*i.e.*, myopia, hyperopia, and astigmatism). Such lenses

are placed on a support fixed to a UV filter attached to the main lens. Figure 4.5(a) shows the camera with an additional +1.0 diopter lens attached to it. The support can hold up to three additional lenses.

For our simulations, we use a simplified eye model adjusted to the camera's settings to achieve consistent results between them. More specifically, we make sure that the *f-number* (*i.e.*, the ratio of the camera lens' focal length f to the diameter D of its aperture):

$$f_{number} = \frac{f}{D} \quad (4.8)$$

is the same for the camera and the eye model. For the experiments shown in the thesis, we fixed the focal length of the camera's main lens to 18mm (regardless of the use of additional lenses). Thus, for instance, given *f-number* values of 4.0, 4.5 and 5.0, the corresponding camera lens aperture values are 4.5mm, 4.0mm and 3.6mm, respectively. Our simplified eye model (Figure 4.5(b)) has an axial diameter of 18mm. The crystalline lens causes the nodal point **N** to be behind the crystalline. Thus, the eye model's effective focal length is 13.5mm: $f_{eye} = 18mm \times \eta_{eye} = 18mm \times 1.333 = 13.5mm$, where η_{eye} is the index of refraction of the eye. As a result, the eye model's pupil size (equivalent of the camera's lens aperture) needs to be rescaled to maintain the same *f-number* value as the camera. Table 4.1 shows the corresponding values of the equivalent camera apertures and pupil diameters. The simulation results shown in Chapter 5 were obtained for $f/5.0$ (third row of Table 4.1), although other values could have been used.

Table 4.1 – Camera apertures and pupil diameters for various f-numbers.

f-number	DSLR Camera (18mm focal length)	Synthetic Eye (13.5mm focal length)
	aperture	pupil diameter
$f/4.0$	4.5mm	3.4mm
$f/4.5$	4.0mm	3.0mm
$f/5.0$	3.6mm	2.7mm

4.4.1 Vertex Distance and Ray Transfer Matrix

The optical power of a lens prescribed for correcting low-order aberrations varies according to the distance from the lens to the cornea, also known as *vertex distance* (Figure 4.6(a)). To compensate for the spacing between camera's main lens and the additional ones (Figure 4.6(b)), we use a *ray transfer matrix* (RTM) formulation (GLYTSIS, 2014). The RTM representing two thin lenses separated by a distance d can be obtained multiplying three matrices: a thin lens matrix (that approximates the DSLR's optical system by a single thin lens), a distance d propa-

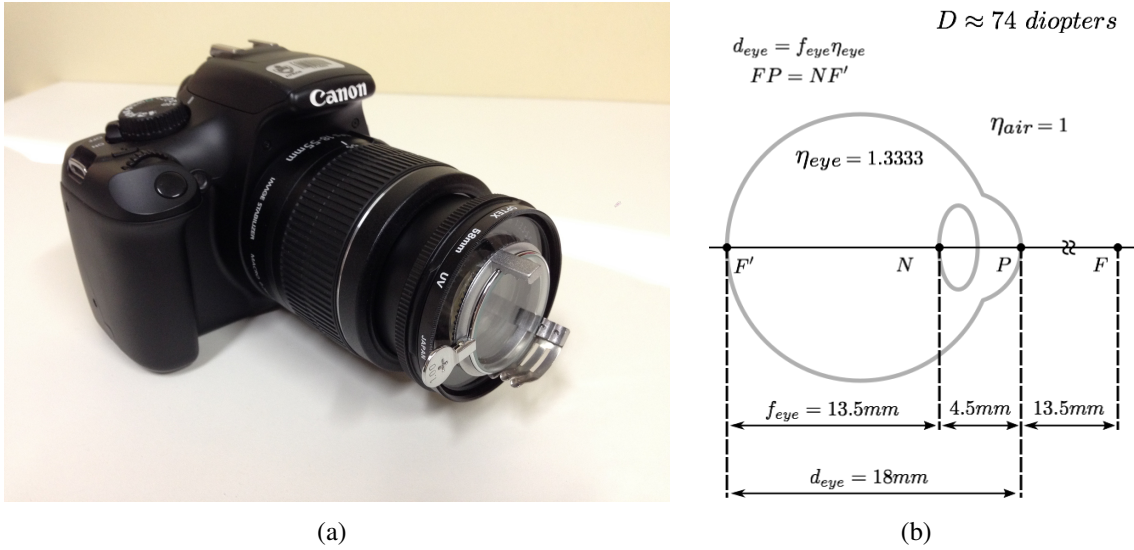


Figure 4.5 – Optical systems used in the validation process: (a) Canon EOS Rebel T3 with apparatus to add up to three extra lenses. Focal lens set to 18mm. (b) Simplified eye model with effective focal length of 13.5mm. \mathbf{N} is the nodal point.

gation matrix, and a thin lens matrix representing our additional lenses:

$$\begin{bmatrix} A_{TL} & B_{TL} \\ C_{TL} & D_{TL} \end{bmatrix} = \begin{bmatrix} 1 & 0 \\ -\frac{1}{f_{camera}} & 1 \end{bmatrix} \begin{bmatrix} 1 & d \\ 0 & 1 \end{bmatrix} \begin{bmatrix} 1 & 0 \\ -\frac{1}{f_{lens}} & 1 \end{bmatrix} = \begin{bmatrix} 1 - \frac{d}{f_{camera}} & d \\ \left(\frac{d}{f_{lens}} - 1 \right) - \frac{1}{f_{camera}} & 1 - \frac{d}{f_{lens}} \end{bmatrix}. \quad (4.9)$$

Here f_{camera} is the DSLR camera focal length (*i.e.*, 18mm in our case), and f_{lens} is the focal length of the (combined set of) additional lens(es). The image captured by the resulting optical

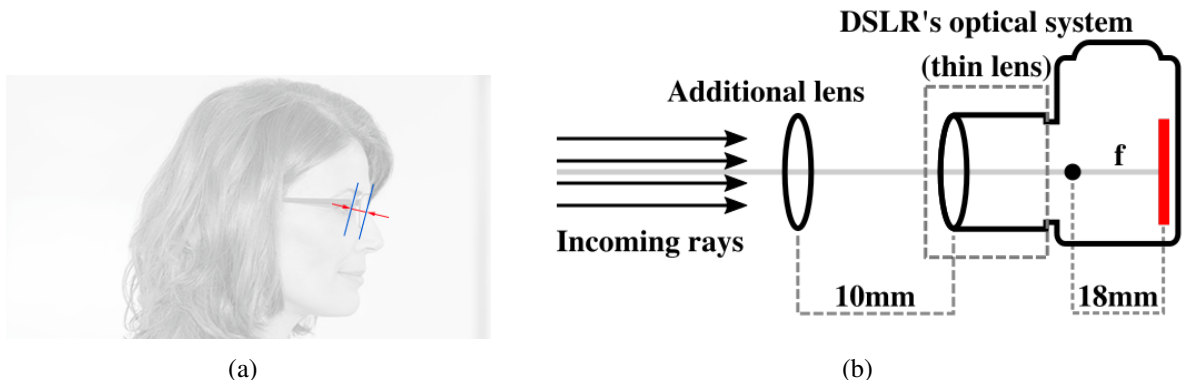


Figure 4.6 – Vertex distance. (a) Typical eyeglasses vertex distance of 12mm. (b) Our camera setup with a distance of 10mm between DSLR's main lens and the additional one.

system is formed at a distance x behind the DSLR camera's optical system. Assuming we want to capture the image of an infinitely far away object (e.g., at distance $s = 10^{20}$ mm from the camera), the overall RTM can be computed as:

$$\begin{bmatrix} A & B \\ C & D \end{bmatrix} = \begin{bmatrix} 1 & x \\ 0 & 1 \end{bmatrix} \begin{bmatrix} A_{TL} & B_{TL} \\ C_{TL} & D_{TL} \end{bmatrix} \begin{bmatrix} 1 & s \\ 0 & 1 \end{bmatrix}. \quad (4.10)$$

Since a set of parallel rays (of an infinitely far away object) are focused by a lens to its focal point, one concludes that x should indeed be the focal length $f_{cam+lens}$ of the compounded optical system comprised by the camera's main lens plus the additional one. By letting $B = 0$, one can solve for x , obtaining:

$$x = f_{cam+lens} = \frac{(d+s) \times (f_{camera} \times f_{lens}) - (d \times f_{lens} \times s)}{(d - f_{lens}) \times f_{camera} + (f_{camera} + f_{lens} - d) \times s}. \quad (4.11)$$

Since 1 diopter = 1/meter, and $f_{cam+lens}$ is expressed in mm, the dioptric power of the resulting compounding optical system is given by:

$$diopt_{cam+lens} = \frac{1}{f_{cam+lens} \times 10^{-3}} = \frac{10^3}{f_{cam+lens}} D. \quad (4.12)$$

Table 4.2 shows the actual increase in dioptric power that result from placing additional lenses with different powers in front of the camera's main lens, considering a vertex distance of 10mm. Thus, for instance, when placing a +1.0D lens in front of the camera's main lens, we are in fact inducing myopia of 1.0101D. Therefore, in order to obtain an image comparable to the one captured by the camera, our simulation should compute a wavefront aberration corresponding to 1.0101D of myopia.

Table 4.2 – Actual increase in dioptric power obtained by placing additional lenses with various powers in front of the camera's main lens considering a vertex distance of 10mm.

Additional Lens' dioptric power	Actual dioptric power
0.0000 D	0.0000 D
1.0000 D	1.0101 D
2.0000 D	2.0408 D
3.0000 D	3.0928 D
4.0000 D	4.1667 D

4.4.2 Comparison of Simulated Results with Ground Truth

This section compares our simulated results with an optical ground truth, obtained by capturing images of the LogMAR charts shown in Figure 4.3. Whenever we reference to the dioptic power of additional lenses, our simulations account for the values described in Table 4.2. To objectively evaluate the quality of the simulated results, we use three objective metrics: the Structural Similarity Image Metric (SSIM) (WANG et al., 2004), the Peak Signal-to-Noise Ratio (PSNR), and the Absolute Difference (AD) of the pixelwise differences between the captured and simulated images. The SSIM metric measures image degradation perceived as change in structural information. It is calculated for each pixel of a given image with respect to some reference image, based on its relationship to other pixels in an 11-by-11 neighborhood. PSNR is a popular metric in image processing for assessing the quality of image reconstruction and compression. It is often expressed using a decibel scale, and computed as

$$PSNR = 10 \log_{10} \left(\frac{peakval^2}{MSE} \right), \quad (4.13)$$

where

$$MSE = \frac{1}{mn} \sum_{i=0}^{m-1} \sum_{j=0}^{n-1} (I_{ref}(i, j) - I(i, j))^2, \quad (4.14)$$

and I is an image being compared to a reference image I_{ref} , both with the same dimensions $m \times n$. $peakval$ is the maximum possible value for a pixel. For instance, for a grayscale image using 8-bits per pixel, $peakval = 255$.

The optical simulation described in this thesis was implemented using MATLAB Student Version (R2014a). Figures 4.7 and 4.8 compare images of a letter from the LogMAR charts with white and black background, respectively, captured by the DSLR camera (top row) against the results of our simulations (second row). The images in the top rows were captured by the camera with extra lenses, ranging from 0 to +4 diopters, in steps of 1 diopter. The second rows show the images produced using our simulation and considering the adjustments in dioptic power required to account for the 10mm spacing between the camera's main lens and the additional one (Table 4.2). Our simulations were applied to the image captured by the camera without any extra lens (*i.e.*, camera +0.00 D). The third and fourth rows of these figures show visual representations of the SSIM and AD metrics, respectively.

Tables 4.3 and 4.4 show the numerical results of the SSIM and PSNR metrics for the results presented in Figures 4.7 and 4.8, respectively. Each row represents the value of a specific metric (*i.e.*, SSIM or PSNR) when comparing an image captured by the DSLR camera with

the one obtained using our simulation. The values of the SSIM metric range from -1.0 (poor similarity) to 1.0 (high similarity). In these tables, one can see that all values are very close to 1.0, indicating that our simulations indeed produce results that are structurally very similar to the ground truth. The PSNR values also indicate that our simulations also produce results very similar to the ground truth. Note that PSNR values of 34.0 decibels and above indicate that two images are essentially indistinguishable from each other.

Figures 4.9 and 4.10 provide similar comparisons for hyperopic vision. The results in the top row were captured with a DSLR camera and extra lenses ranging from 0 to -4 diopters,

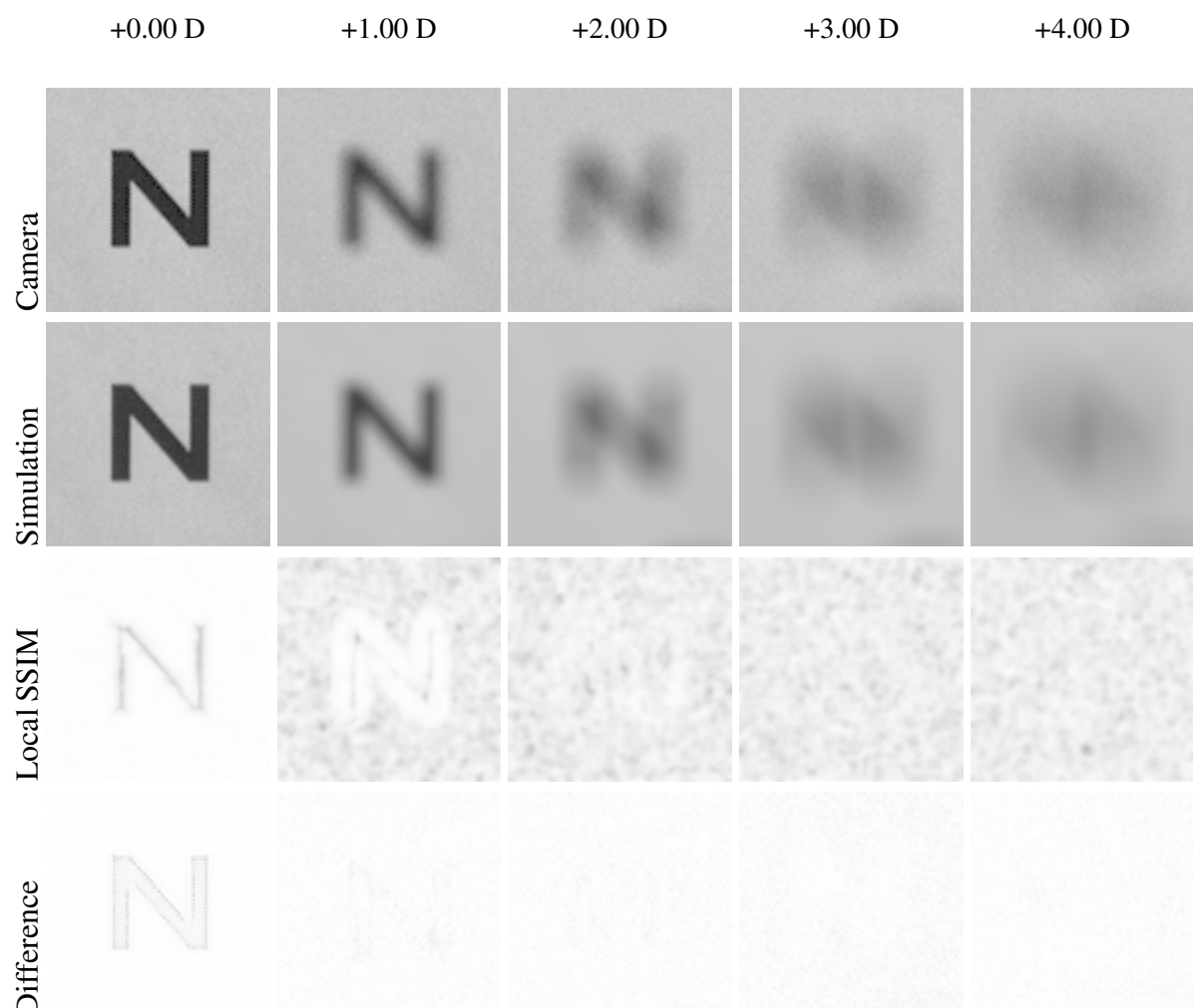


Figure 4.7 – Comparisons of our simulated results against ground truth obtained with a myopic camera. These large images correspond to a Snellen ratio of 20/200. (top row) Images captured using the DSLR camera with extra lenses varying from 0.0 to 4.0 diopters. (second row) Our simulated results. (third row) SSIM metric results. (fourth row) AD metric.

Table 4.3 – SSIM and PSNR table of myopic perception (Figure 4.7)

	+0.00 D	+1.00 D	+2.00 D	+3.00 D	+4.00 D
SSIM	0.9834	0.9384	0.9428	0.9484	0.9490
PSNR	34.6491	35.7883	33.8015	35.2325	33.2118

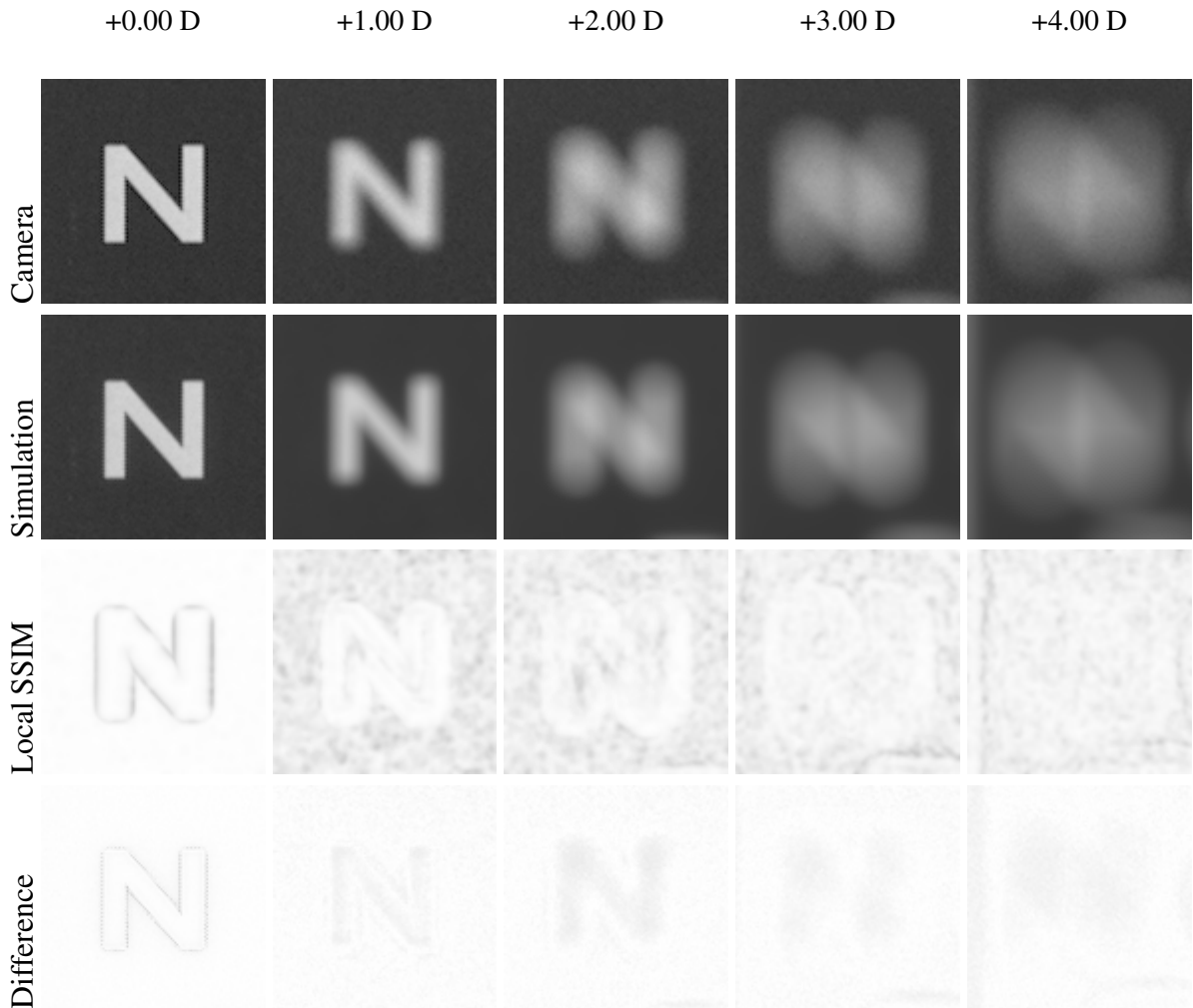


Figure 4.8 – Comparisons of our simulated results against ground truth obtained with a myopic camera. These images correspond to a Snellen ratio of 20/200. (top row) Images captured using the DSLR camera with extra lenses varying from 0.0 to 4.0 diopters. (second row) Our simulated results. (third row) SSIM metric results. (fourth row) AD metric.

in steps of -1 diopter. The second rows show our simulated results. Likewise, the third row presents the visualization of the pixel-by-pixel SSIM index when comparing the captured and simulated hyperopic results, and the bottom one presents the absolute difference of images. Tables 4.5 and 4.6 provide the SSIM and PSNR values comparing the simulated images to the ground truth, attesting the quality of our results.

Table 4.4 – SSIM and PSNR table of myopic perception (Figure 4.8)

	+0.00 D	+1.00 D	+2.00 D	+3.00 D	+4.00 D
SSIM	0.9869	0.9378	0.9324	0.9296	0.9322
PSNR	34.7779	38.8748	38.7219	35.6993	39.3720

Table 4.5 – SSIM and PSNR table of hyperopic perception (Figure 4.9)

	-0.00 D	-1.00 D	-2.00 D	-3.00 D	-4.00 D
SSIM	0.9869	0.9192	0.9149	0.9119	0.9130
PSNR	34.7778	34.3781	32.8601	32.6680	29.5003

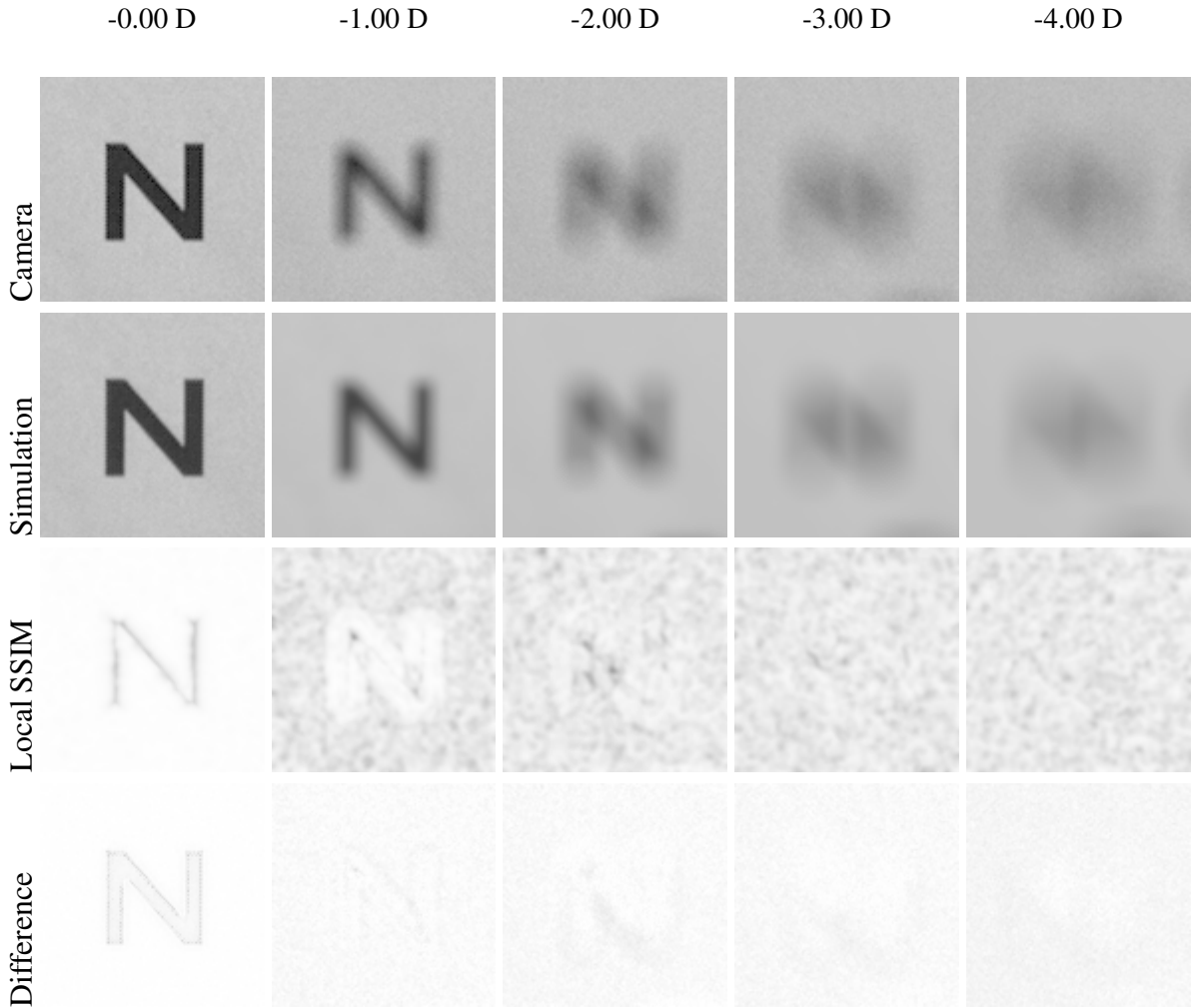


Figure 4.9 – Comparisons of our simulated results against ground truth obtained with a hyperopic camera. These large images correspond to a Snellen ratio of 20/200. (top row) Images captured using the DSLR camera with extra lenses varying from 0.0 to -4.0 diopters. (second row) Our simulated results. (third row) SSIM metric results. (fourth row) AD metric.

Besides simulating the effects of defocus (*i.e.*, myopia and hyperopia), we have also compared the results of our simulation for astigmatic vision. This is illustrated in Figures 4.11 and 4.12. The Sloan letters in Figure 4.11 were captured by the DSLR camera with an additional cylindrical lens with -2.0 diopters, rotated in order to simulate astigmatism in the horizontal meridian ($\phi = 90^\circ$). Similarly, Figure 4.12 shows the real and simulated astigmatism in the vertical meridian ($\phi = 180^\circ$). Figures 4.13 and 4.14 show the captured and simulated results for a cylindrical lens with +2.0 diopters. Tables 4.7 and 4.8 show the results of the SSIM and PSNR metrics for these astigmatic results. Again, the SSIM indices are close 1.0 and the PSNR

Table 4.6 – SSIM and PSNR table of hyperopic perception (Figure 4.10)

	-0.00 D	-1.00 D	-2.00 D	-3.00 D	-4.00 D
SSIM	0.9833	0.9157	0.9196	0.9213	0.9165
PSNR	34.6438	35.0465	36.6722	33.3992	30.9853

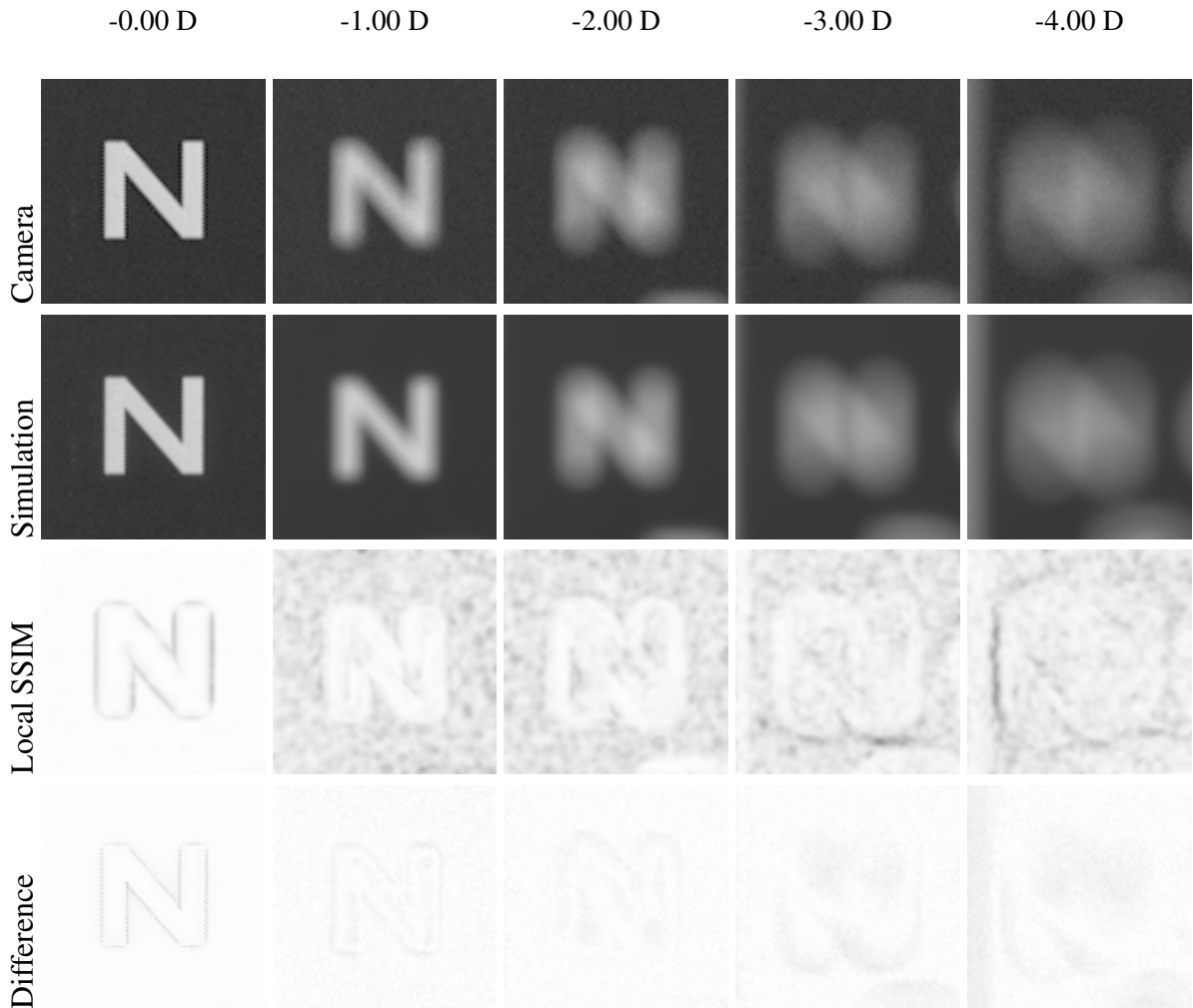


Figure 4.10 – Comparisons of our simulated results against ground truth obtained with a hyperopic camera. These images correspond to a Snellen ratio of 20/200. (top row) Images captured using the DSLR camera with extra lenses varying from 0.0 to 4.0 diopters. (second row) Our simulated results. (third row) SSIM metric results. (fourth row) AD metric.

is close to or above 34.00 decibels.

Note that for the astigmatic results, part of the differences visible in the astigmatic local SSIM index visualizations (Figures 4.11, 4.12, 4.13 and 4.14) is due to the difficulty of a precise manual alignment of the astigmatic axes to the ones used in our simulations. Any deviation from the simulated angles affects the results of the quality metric.

Figures 4.15 and 4.16 compare the results of our simulations with the images captured by a myopic camera (additional lens of +2.0 D) when looking to several 20/200 Sloan letters

Table 4.7 – SSIM and PSNR table of the negative astigmatic perception.

		N	C	K	Z	O
-2.00 @90	SSIM	0.9171	0.9174	0.9193	0.9242	0.9185
-2.00 @90	PSNR	36.4269	36.0369	37.0615	35.9831	36.9738
-2.00 @180	SSIM	0.9169	0.9207	0.9226	0.9220	0.9201
-2.00 @180	PSNR	34.6329	37.8456	37.4705	38.7289	37.8041

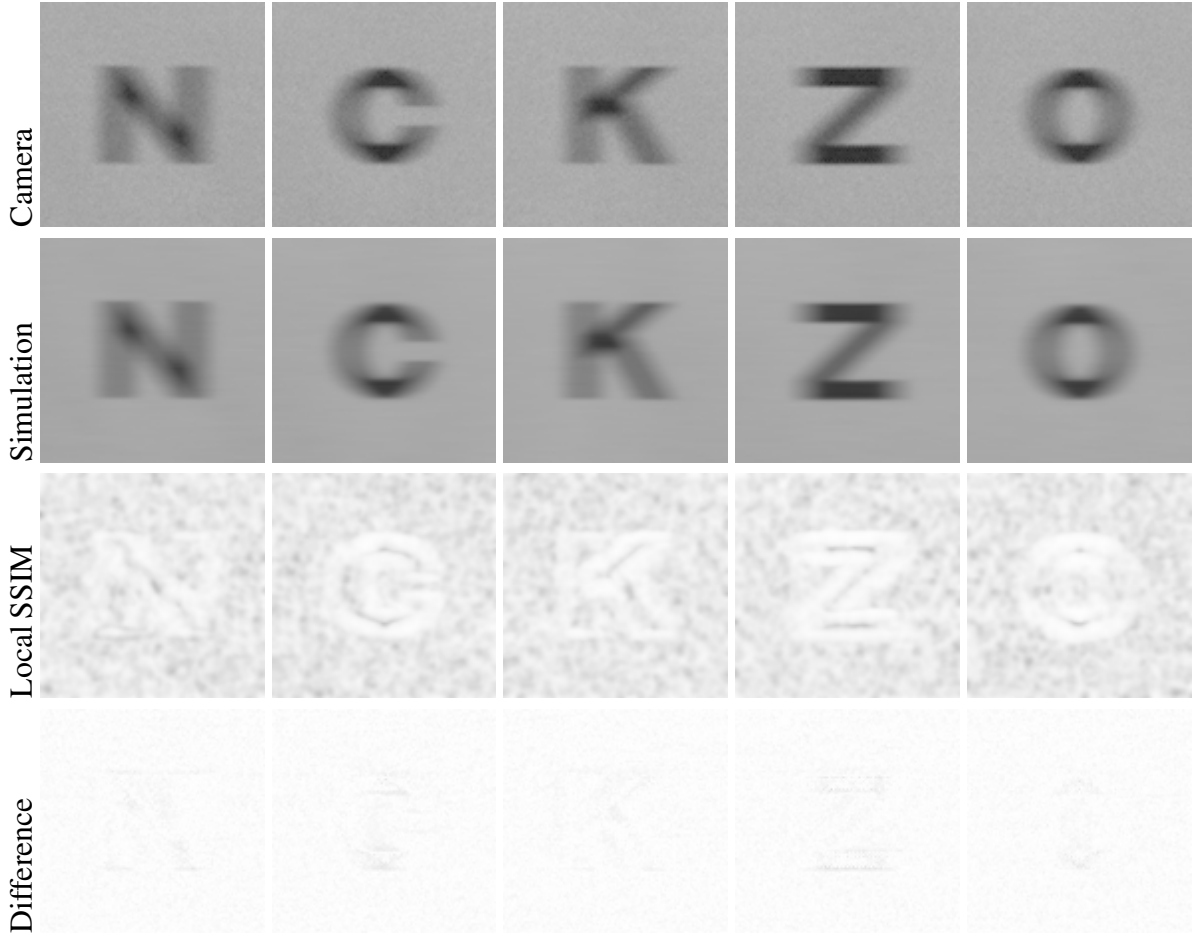


Figure 4.11 – Comparisons of our simulated results against ground truth obtained with an astigmatic camera. These large images correspond to a Snellen ratio of 20/200. (top row) Images captured using the DSLR camera with an extra cylindrical lens with -2 diopters at the vertical meridian. (second row) Our simulated results. (third row) SSIM metric results. (fourth row) AD metric.

from a distance of three feet. The first column shows synthetic Sloan letters used as input to produce the simulated results shown in the second column (*Synthetic Simulation*). The last three columns show, respectively, images captured by the DSLR camera, images captured by the DSLR camera with an additional +2.0 D lens, and the results of our simulations for +2.0408 D (see Table 4.2) of myopia applied to the images shown in the column *Camera Capture*.

Our technique can be used to simulate arbitrary wavefront aberrations, given the corresponding aberration function $W_{(x,y)}$ (Equation 4.3). Thus, even though such a validation depends on the existence of an optical ground truth, the method is not limited to what can be modeled

Table 4.8 – SSIM and PSNR table of the positive astigmatic perception.

		N	C	K	Z	O
+2.00 @90	SSIM	0.9307	0.9271	0.9277	0.9193	0.9303
	PSNR	37.2835	35.4130	36.3713	32.7150	36.2564
+2.00 @180	SSIM	0.9235	0.9287	0.9257	0.9308	0.9260
	PSNR	33.3036	36.8478	35.0677	36.5272	36.2953

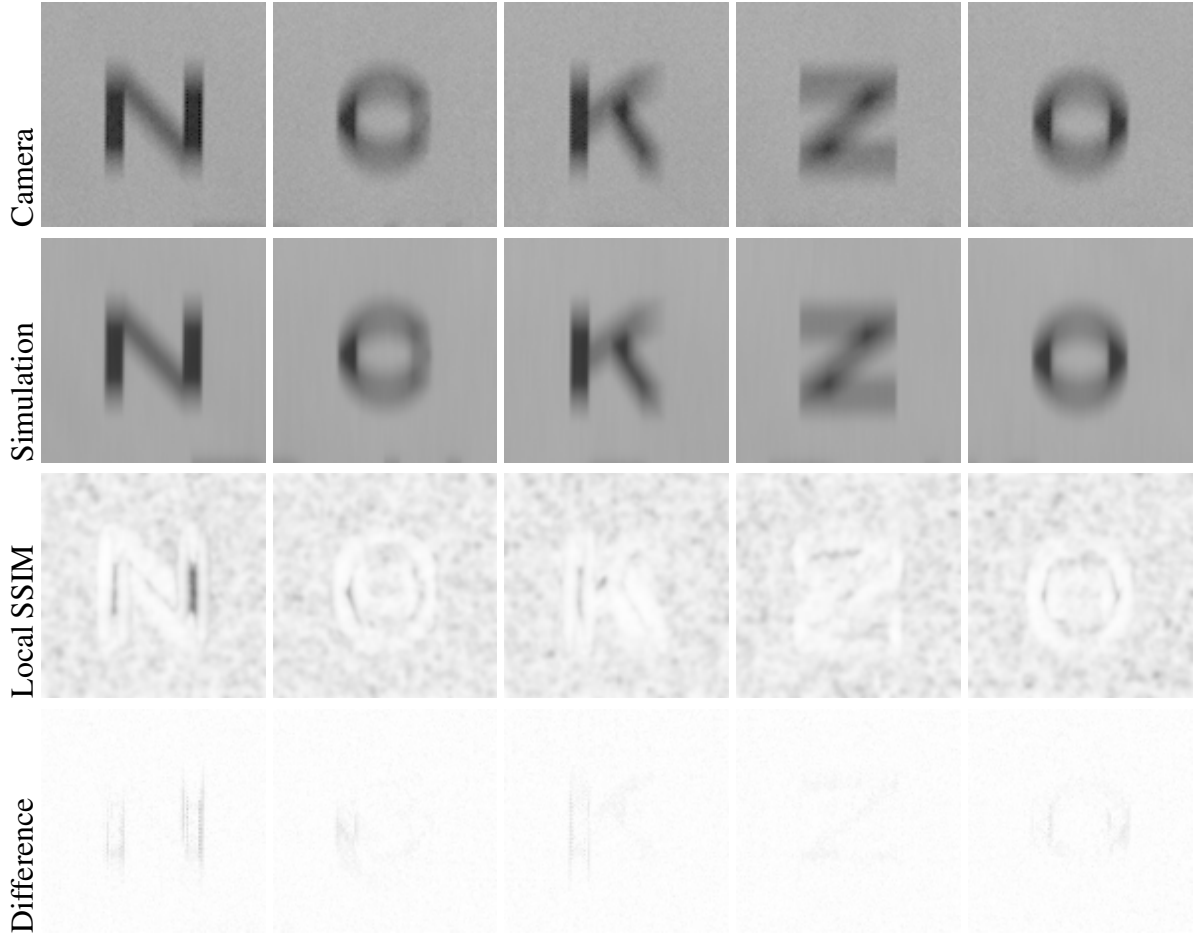


Figure 4.12 – Comparisons of our simulated results against ground truth obtained with an astigmatic camera. These large images correspond to a Snellen ratio of 20/200. (top row) Images captured using the DSLR camera with extra cylindrical lens with -2 diopters at the horizontal meridian. (second row) Our simulated results. (third row) SSIM metric results. (fourth row) AD metric.

using a DSLR camera and additional lenses. Columns *Aberrated Wavefront* and *Spatial PSF* in Figure 4.17 show the normalized aberrated wavefront and the spatial PSF associated with the simulation results shown in the last column for a given input letter. Its top row shows how a combination of low-order aberrations (myopia and astigmatism) affects the perception of a Sloan letter. The second and third rows simulate, respectively, higher values of pure astigmatism and spherical aberration than one can capture with the lenses available in our trial lens set. Finally, the bottom row shows the results of a simulation involving only higher-order aberrations.

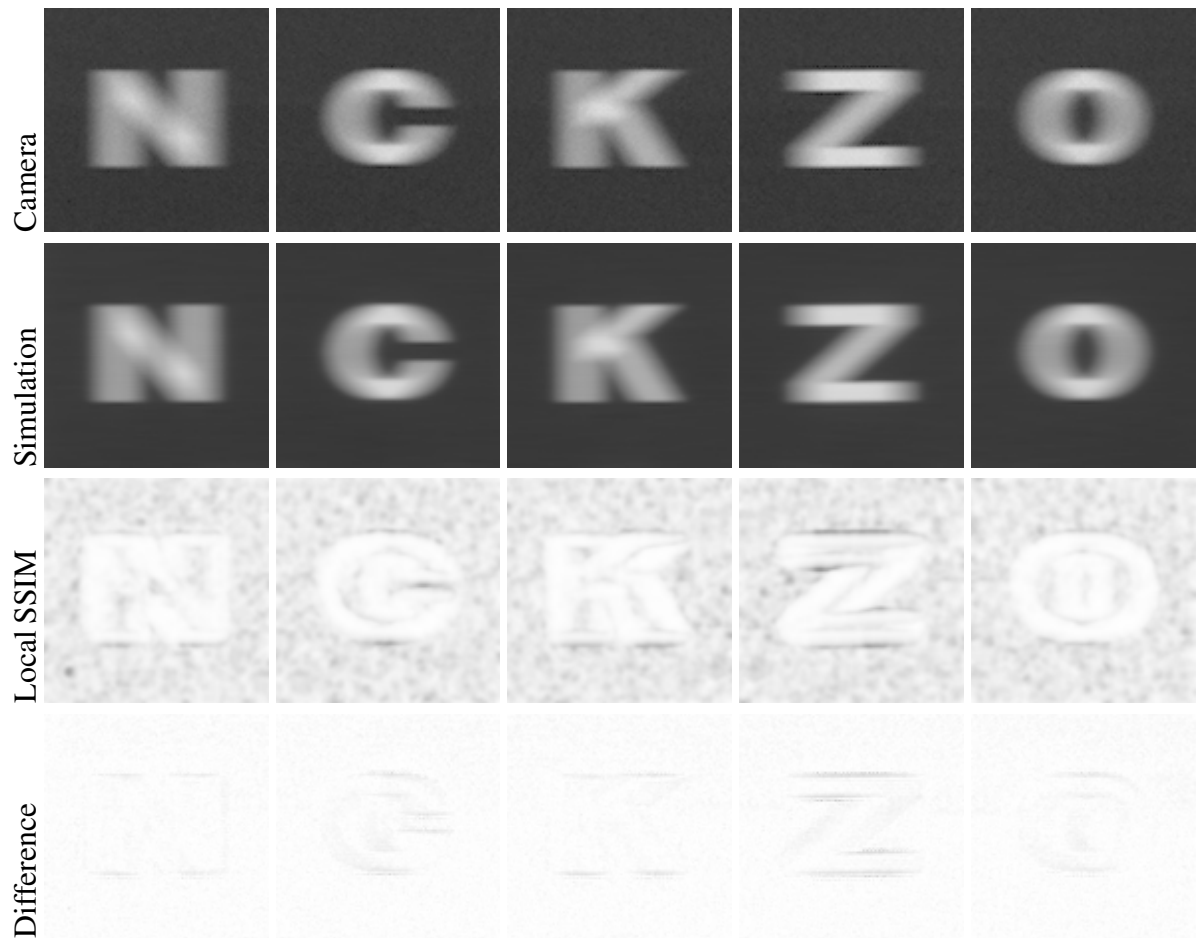


Figure 4.13 – Comparisons of our simulated results against ground truth obtained with a astigmatic camera. These images correspond to a Snellen ratio of 20/200. (top row) Images captured using the DSLR camera with an extra cylindrical lens with 2 diopters at the vertical meridian. (second row) Our simulated results. (third row) SSIM metric results. (fourth row) AD metric.

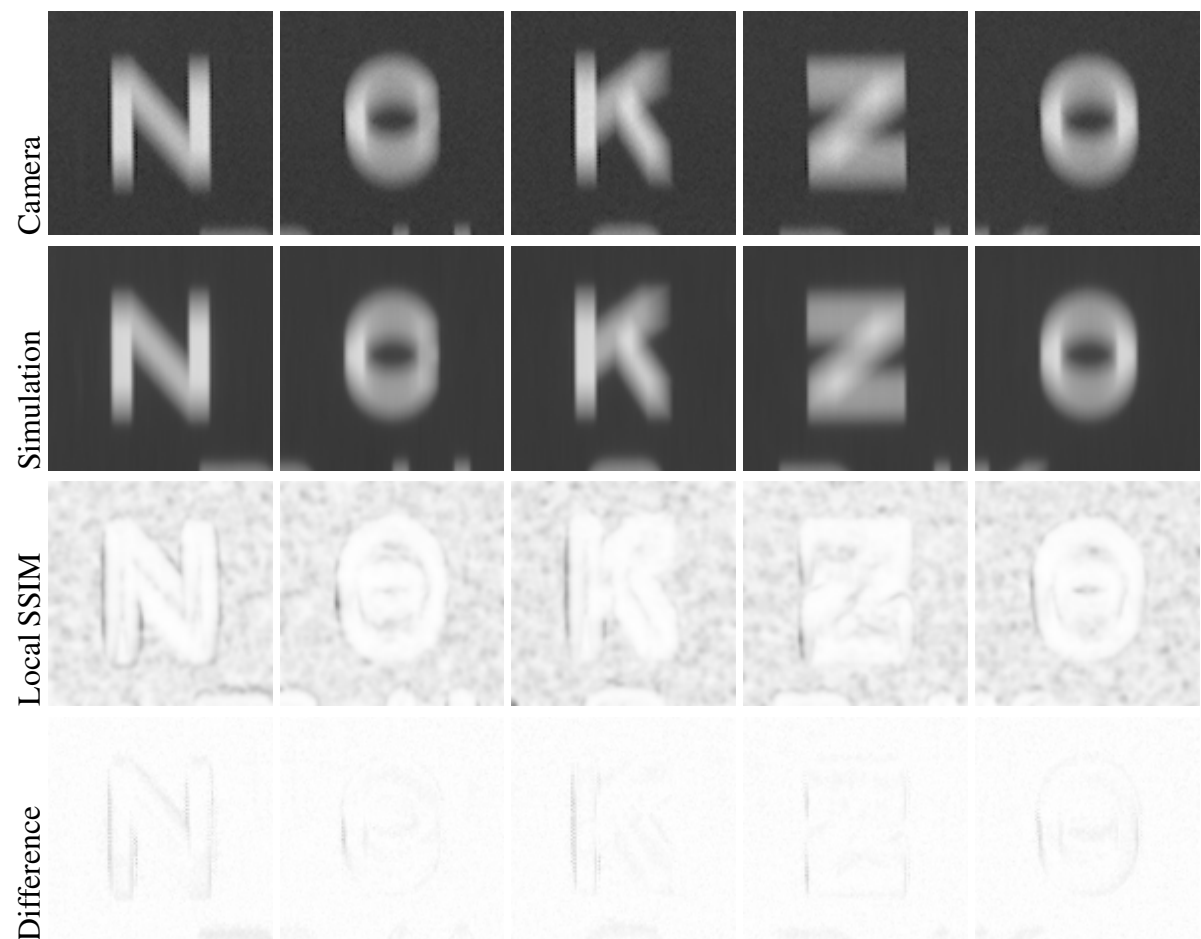


Figure 4.14 – Comparisons of our simulated results against ground truth obtained with a astigmatic camera. These images correspond to a Snellen ratio of 20/200. (top row) Images captured using the DSLR camera with an extra cylindrical lens with 2 diopters at the horizontal meridian. (second row) Our simulated results. (third row) SSIM metric results. (fourth row) AD metric.

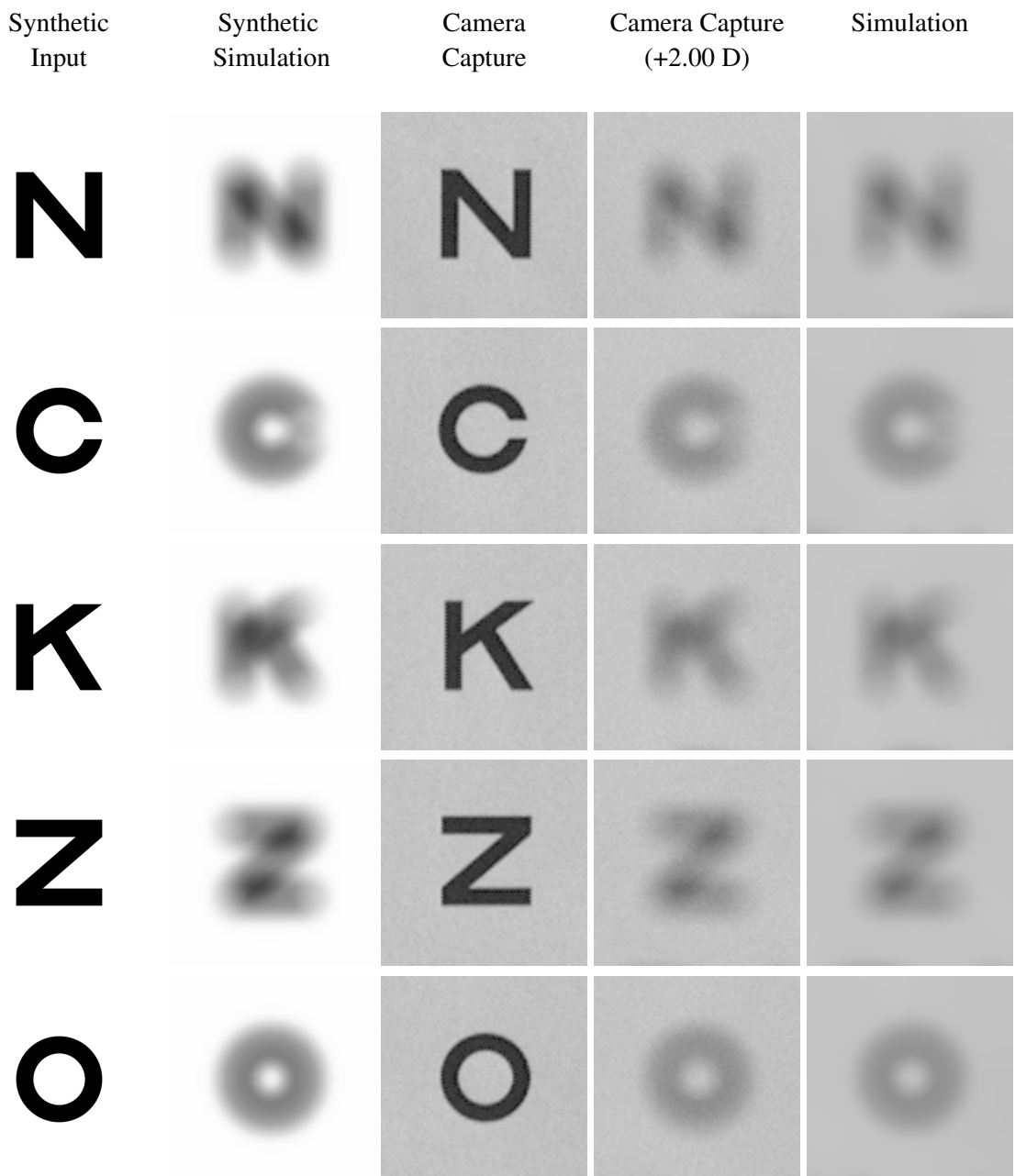


Figure 4.15 – Comparisons of our simulated results against ground truth obtained with a myopic camera. The first two columns show synthetic images and the results of their simulations for +2.0408 D of myopia. The last three columns show, respectively, images captured by the DSLR camera, images captured by the DSLR camera with an additional +2.0 D lens, and the results of our simulations for +2.0408 D of myopia applied to the images shown in the column *Camera Capture*.

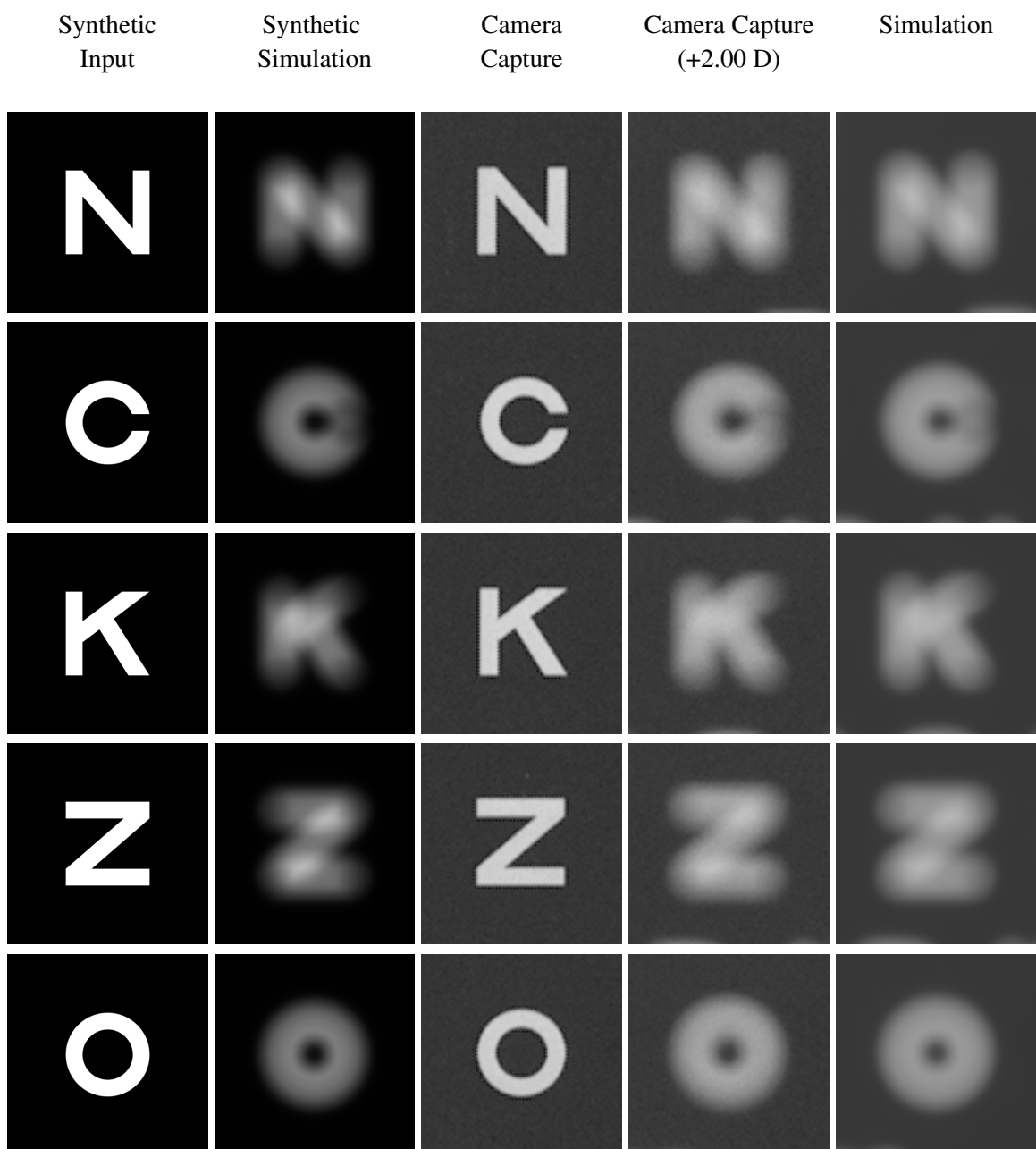


Figure 4.16 – Comparisons of our simulated results against ground truth obtained with a myopic camera. The first two columns show synthetic images and the results of their simulations for +2.0408 D of myopia. The last three columns show, respectively, images captured by the DSLR camera, images captured by the DSLR camera with an additional +2.0 D lens, and the results of our simulations for +2.0408 D of myopia applied to the images shown in the column *Camera Capture*.

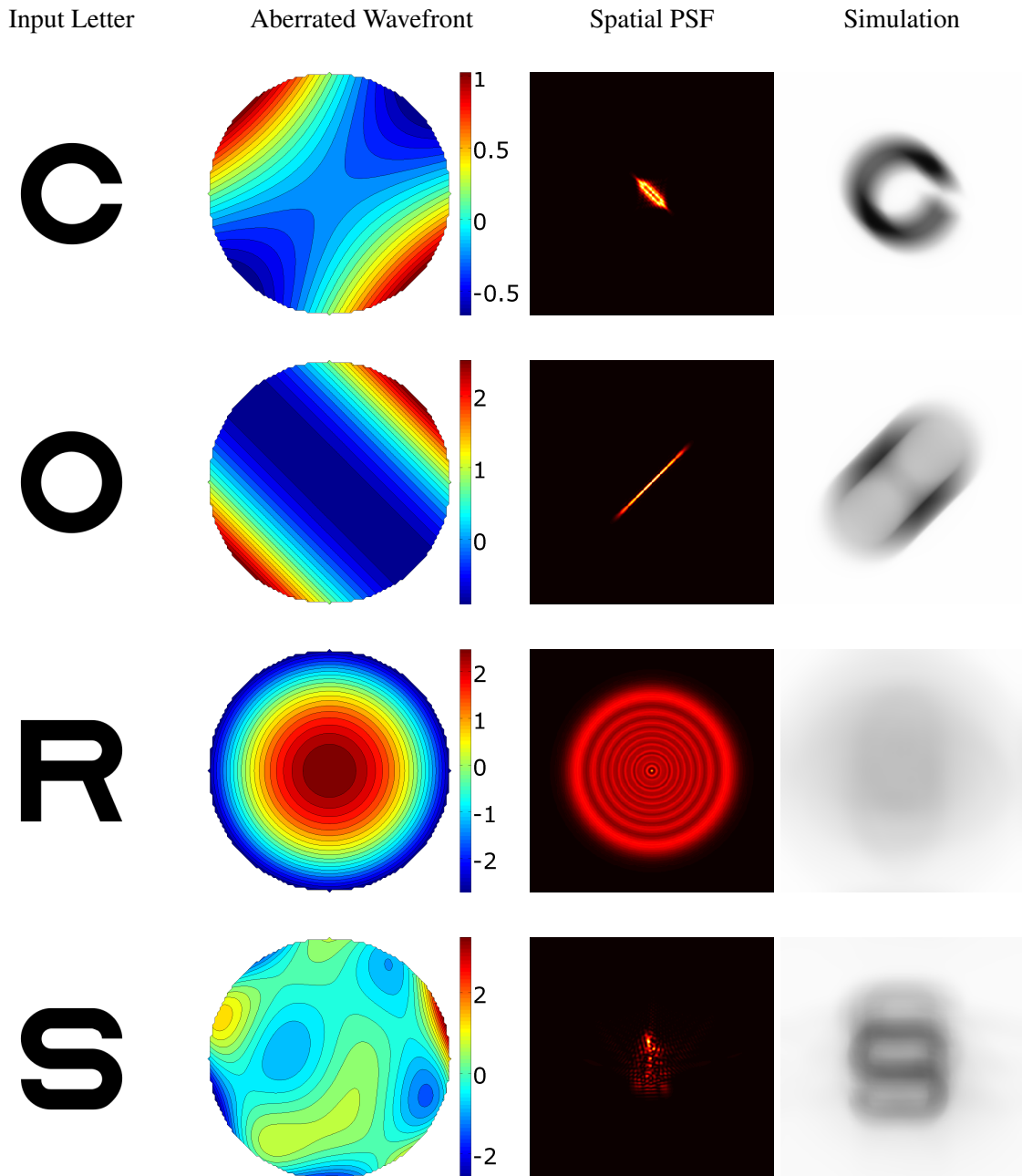


Figure 4.17 – Simulations with arbitrary wavefronts. The input letter images correspond to a Snellen ratio of 20/200. (second column) Normalized aberrated wavefront. (third column) The spatial PSF. (fourth column) Our simulation results given the images shown in column *Input Letter*. The top row shows how a combination of low-order aberrations (+0.5 Sph. -2.0 Cyl. at 45) affects the perception of a Sloan letter. The second and third rows simulate, respectively, higher values of pure astigmatism and spherical aberration (-4.7 Cyl. at 135 and +6 Sph.) than one can capture with the lenses available in our trial lens set. The bottom row shows the results of a simulation involving only higher-order aberrations ($Z_3^{-3} = 0.2$, $Z_3^{-1} = 0.2$, $Z_3^3 = 0.1$, $Z_4^2 = 0.2$, $Z_5^{-5} = 0.4$, $Z_5^1 = 0.3$).

4.5 Summary

This chapter described the visual simulation technique that represents one of the central aspects of this thesis. For this, we have presented all the involved mathematical and optical concepts. The chapter also presented a validation of our simulation technique by comparing its results with images captured by a camera instrumented with additional lenses to induce myopia, hyperopia, and astigmatism. The results of the SSIM and PSNR metric confirm that the results produced by our simulations are structurally and perceptually similar to the ground truths captured by the camera.

5 ABSOLUTE THRESHOLD FOR VISION

In addition to the previously discussed optical aberrations that affect visual perception, there are non-optical characteristics (*i.e.*, intrinsic individual phenomena) that could be considered in the simulation to achieve more realistic renderings of retinal images. In this section, we discuss an attempt to estimate one such intrinsic characteristic — the *absolute threshold for vision* or simply *absolute threshold* or *minimum visible*. The light emitted/reflected by an out-of-focus scene point is spread out across some area of the observer's retinal surface, producing a so-called *circle of confusion* and causing blur (Figure 5.1). Since the eye's photoreceptors have an energy threshold for triggering a neural signal indicating light detection, the larger the circle of confusion (and consequent spread of the incoming energy), the bigger should be the light intensity required to trigger such neural signal. Thus, considering an individual without any condition that reduces the translucency of the eye along its optical path (*e.g.*, cataracts), we have formulated the following hypothesis: **H1** *The absolute threshold for vision is directly proportional to the magnitudes of the eye's defocus (i.e., myopia or hyperopia) and astigmatism. As such, the absolute threshold can be used as an estimate of the spherical equivalent of the eye's refractive error.* The *spherical equivalent* is the sum of the spherical (defocus) plus half of the cylindrical (astigmatism) values of the optical system (*i.e.*, $S + 0.5 \times C$) expressed in diopters.

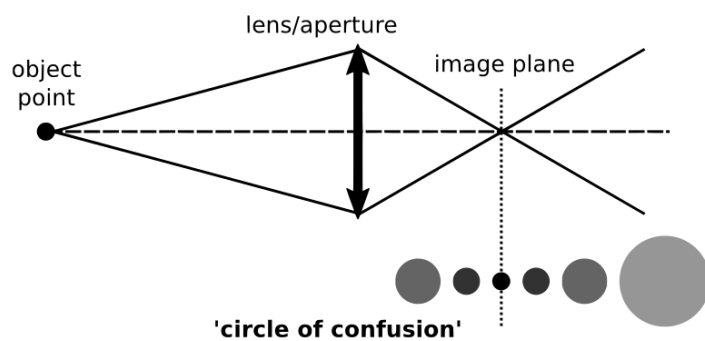


Figure 5.1 – The image of an in-focus point is formed on the image plane. An out-of-focus point, on the other hand, projects a so-called circle of confusion on the image plane, causing blur. The radius of the circle is proportional to the amount of defocus.

The following subsections discuss a psychophysical experiment established to estimate the absolute threshold information of an eye. The population sample is presented together with the quasi-random algorithm used during the experiments.

5.1 Experimental Design

In order to verify the correlation between the absolute threshold and defocus, we have prepared a controlled experiment (Figure 5.2). All participants were informed about the risks, burdens, and benefits of the research. Next, all participants had their vision assessed (under the supervision of an ophthalmologist) without and with the use of cycloplegic eyedrops. First, their vision assessed using an autorefractor (model KR-8900, by TOPCON), which is an instrument routinely used for automatically performing objective refraction tests (*i.e.*, estimating low-order refractive errors). Then, each subject received one drop of a cycloplegic eyedrop in each of the eyes, and after 15 minutes, the autorefractor test was repeated. As the cycloplegic drug relaxes the ciliary muscles, which are responsible for allowing the eye to focus at different distances. A cycloplegic drug can be used to relax the ciliary muscles (*i.e.*, avoid accommodation), forcing the eye to focus at infinity. Complete relaxation, however, requires relatively-high concentrations of the drug.

For the psychophysical experiment, each subject performed three evaluations to establish his/her absolute threshold for vision. The first psychophysical evaluation was applied right after the second vision assessment (under the effect of the cycloplegic eyedrops). The other two evaluations were taken with intervals of at least one day between each other.

All evaluations were performed with naked eye (*i.e.*, the subject were not allowed to use corrective eyeglasses or contact lenses). To obtain a larger and uniformly-distributed sample set, each eye of each subject was tested 17 times simulating various degrees of refractive errors. For this, we added (to the experimental device) external lenses with integer powers ranging from -5.0 D ... 0.0 D ... +5.0 D, as well as ± 0.25 D, ± 0.5 D, and ± 1.5 D. The net effect is summing these powers to the original refractive errors of the participants. Between any two tests, there was an interval of approximately thirty seconds. The order in which the lenses were placed in the device was randomly defined for each subject. More details about the experiments are provided in Appendix A.

5.2 Participants

The inclusion criteria for the study are quite inclusive and only stipulate that all participants must be able to perform subjective and objective refraction test, as well as auto-refraction. 23 individuals meeting the inclusion criteria were asked to participate. Three had availability restrictions and were not included in the experiment.

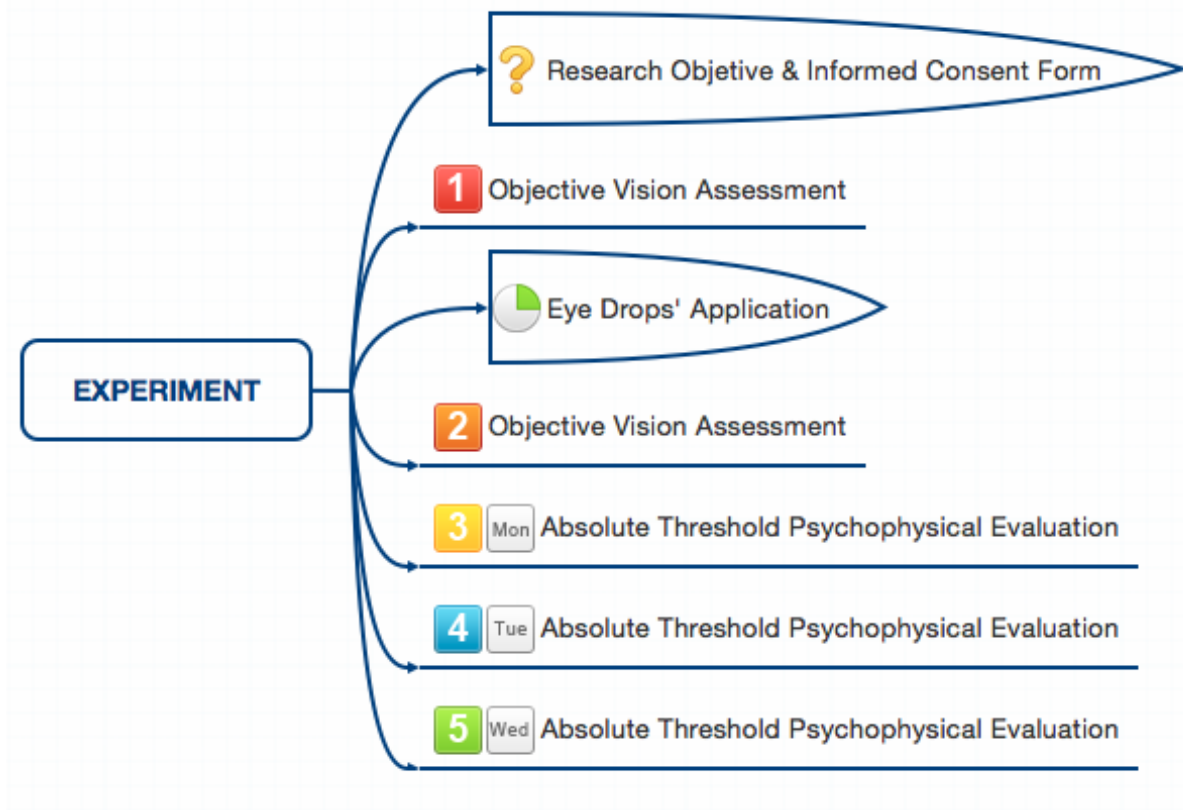


Figure 5.2 – Stages of the Absolute Threshold experiment.

The subjects consisted of 17 males and 3 females, with ages ranging from 23 to 33 years old (mean of 25.3 and standard deviation of 2.51). Out of these, 6 male and the 3 female use corrective eyeglasses, and 1 male uses contact lenses. For these ten individuals, the minimum, maximum, mean, and standard deviation of their spherical error S in diopters were: $S_{min} = -3.5$, $S_{max} = 1.25$, $S_{mean} = -0.275$, and $S_{std} = 1.452$, respectively. Likewise, the minimum, maximum, mean, and standard deviation of their cylindrical error C in diopters were: $C_{min} = -2.5$, $C_{max} = 0.0$, $C_{mean} = -0.625$, and $C_{std} = 0.655$, respectively. Thus, their spherical equivalent refraction (SER) can be summarized as: $SER_{min} = -3.75$, $SER_{max} = 1.25$, $SER_{mean} = -0.5877$, and $SER_{std} = 1.429$. The axis of astigmatism of these subjects, expressed in degrees, can be summarized as: $A_{min} = 0.0$, $A_{max} = 179.0$, $A_{mean} = 57.25$, and $A_{std} = 69.76$. All these measurements were computed from the results of the autorefractor with the use of cycloplegic eyedrops.

5.3 Quasi-Random Algorithm

The algorithm developed to determine the absolute threshold is divided into two major phases. In the first one, the goal is to find a tight interval containing the absolute threshold as

quick as possible. While this can be efficiently performed using a binary search, we adopted a quasi-random strategy to avoid bias among repetitions of the test. In the second phase, the participant uses a slider to precisely determine his/her absolute threshold. The second step could be replaced by a binary search.

Listing 5.1 – Estimating the absolute threshold for vision

```

1 set minimum intensity to zero
2 set maximum intensity to one
3 % Phase 1: determining a tight interval for the absolute threshold
4 do {
5     Randomly get a new intensity value
6         inside [minimum intensity, maximum intensity],
7             in multiples of 0.1
8     turn on a single pixel in the device screen
9     ask if the user see the stimulus
10
11    if stimulus is visible
12        maximum intensity = new intensity
13    else
14        minimum intensity = new intensity
15
16 } while ((maximum intensity - minimum intensity) > 0.1)
17 % Phase 2: absolute threshold determination
18 < user interaction based on a slider >

```

5.4 Measurements

We have designed an auxiliary apparatus to estimate the absolute threshold for vision. The device, built using a 3-D printer, consists of a tube with one of its ends containing a support for lenses and the fixation of an eyecup, while the other end holds a smartphone (Figure 5.5(a)). The eyecup end holds an 8.0 D plano-convex lens, making the length of the tube equal to this lens focal distance (12.5 cm). With such configuration, the light coming from a pixel from the smartphone's screen reaches the subject's eye as a set of parallel rays. Thus, this is equivalent to observing a point at infinity. The eyecup was adapted from a viewfinder of the DSLR camera. The device was completely painted with a dull black paint to avoid reflections in its interior. For the experiments, we have used an iPhone 5 to generate light stimulus and control its intensity.

The iPhone 5 uses a Retina Display ($1,136 \times 640$ pixels) with 326 pixels per inch.

To calibrate the amount of light emitted by the iPhone 5, we used a digital light meter (Minipa, model MLM-1020) placed 3.0 cm from the smartphone's screen (Figure ??). The light meter (luximeter) and the iPhone were connected to a MacBook Pro laptop through USB connections. A program in the laptop controlled the intensity of a single pixel displayed in the central region of the iPhone screen and read the measurement made by the luximeter. The reading of each measurement was made after the pixel intensity has been displayed for five seconds to allow the luximeter enough time to stabilize its reading. At the end of this procedure, we obtained a response curve relating stimulus and lux values.

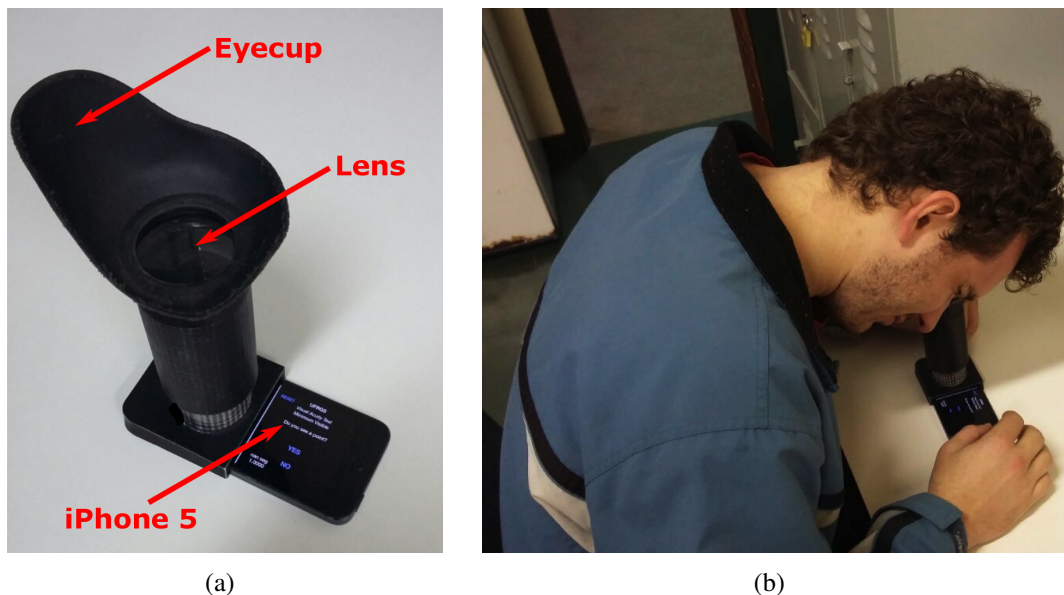


Figure 5.3 – Apparatus designed to help in the absolute threshold psychophysical evaluations

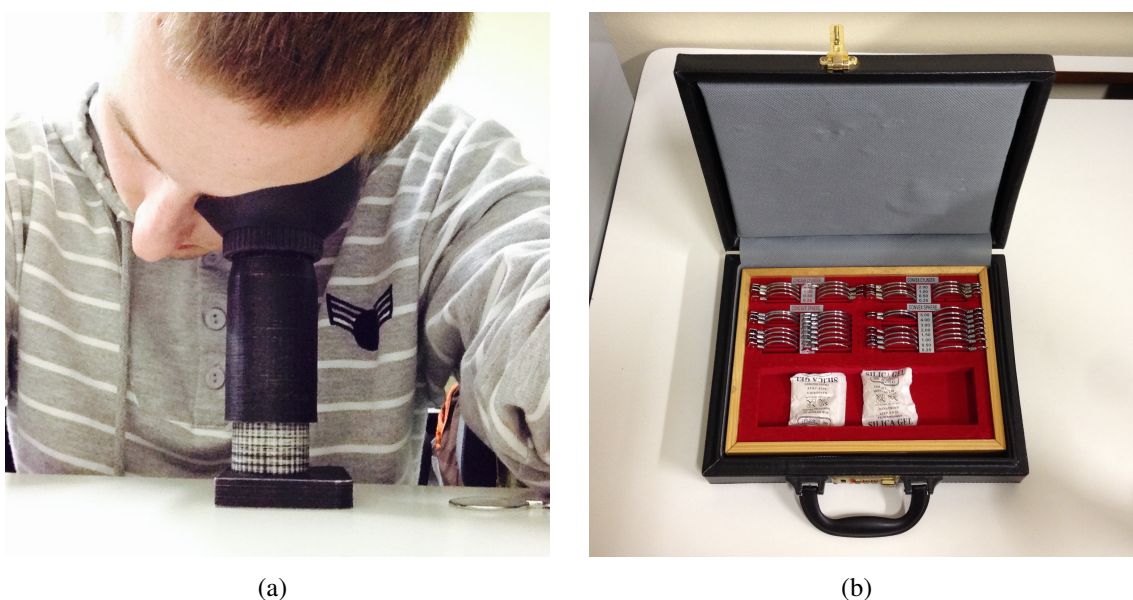


Figure 5.4 – XXX

Medical data from 20 subjects were captured with specialized ophthalmic equipment from a partner clinic. This data is fully described in Appendix ??, together with the results of all absolute threshold psychophysical evaluations. We've realized absolute threshold experiments as described in 5.1, and selected two groups of them to present partial results — from subject 1 (hyperopic) and 11 (myopic). Figure 5.7 presents a plot for each subject that combines the result of four psychophysical experiments. The blue lines represent the minimum amount of light perceived by the individuals when varying additional lenses from -5 to +5 diopters. It also consider the use of eyedrops. The red ones are the mean of three psychophysical experiments without using eyedrops (*i.e.*, crystalline lens can and will accommodate if necessary). The dashed lines stands for the data of the right eye, and the circles indicate the minimum intensity value considering all lenses. At last, the black lines indicate the individual's spherical equivalent refraction.

To better understand the accommodation effects in the absolute threshold determination, we've elaborated a controlled experiment performed by a single subject. We've applied extra drops (3 drops in total) of the cycloplegic eye drop, and evaluated the minimum perceived intensity along time. The results of this experiment are illustrated in Figure 5.8. Figure 5.8(a) shows the apparent effect — mydriasis (*i.e.*, the dilation of the pupil). Due to the high dosage of eyedrops, such effect lasted for 10 days. However, as can be seen in Figure 5.8(b), higher dosages and short time (red line) values almost correspond to the aberration captured by the gold standard ophthalmic equipment.

Considering that absolute threshold values tends to increase according to the lens power,

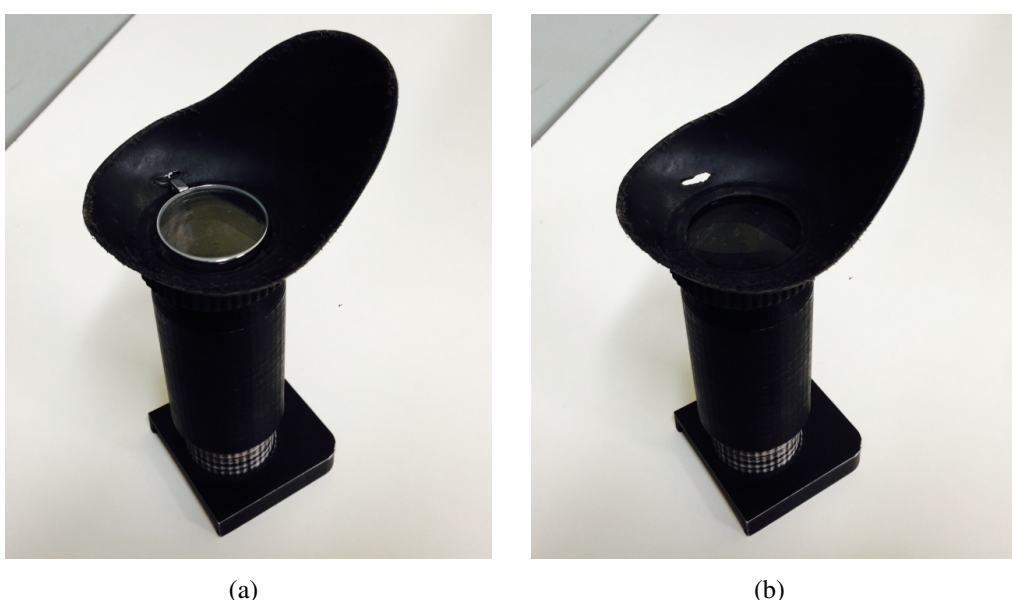
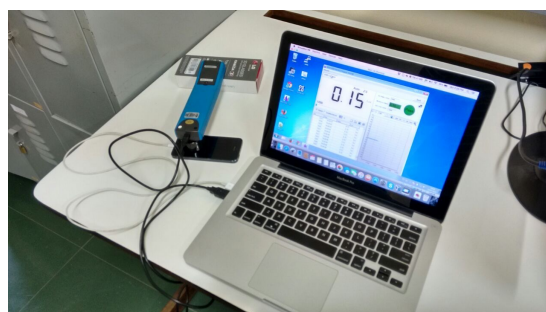


Figure 5.5 – XXX



(a)



(b)

Figure 5.6 – Variations of the apparatus. (a) the interior of the final version; (b) a variant of it designed for the calibration curve acquirement process; and (c) wood device to control camera's distance.

and we've used the least squares fitting techniques to obtain a 2nd order polynomial representation of the individuals absolute threshold. By calculating the correlation-coefficient matrix and evaluate the fit parameters, we can plot and calculate confidence intervals for a predicted response. Such internals (*i.e.*, confidence bounds) are illustrated in red-dashed lines in Figures 5.9 and 5.10. The green lines are the absolute threshold values defined by the psychophysical evaluations using eyedrops (Figures 5.9(a) and 5.10(a)) or not (Figures 5.9(b) and 5.10(b)). The fitted curve is in blue, and its lower value it is represented by a blue circle.

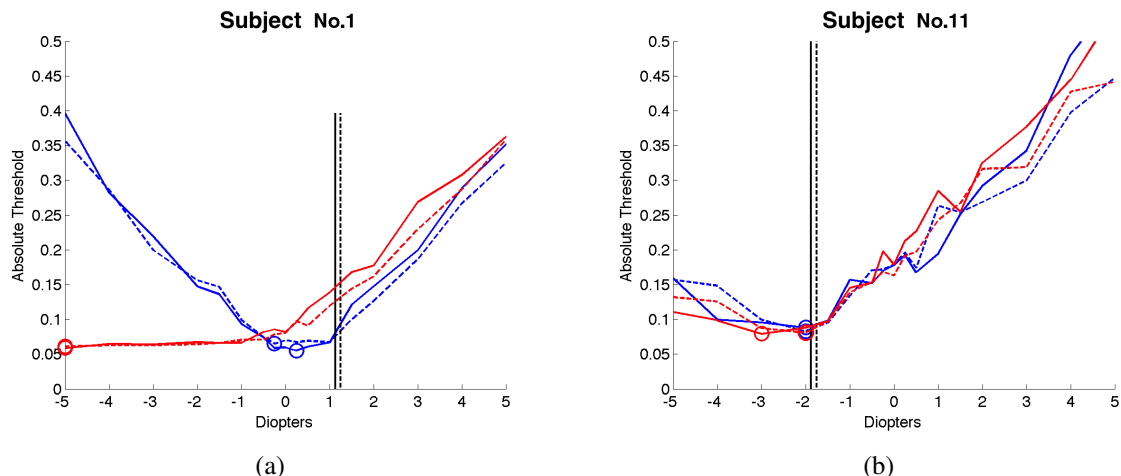


Figure 5.7 – Plot of absolute threshold data acquired with and without eyedrops. (a) a hyperopic subject from the sample; (b) a myopic subject from the sample.

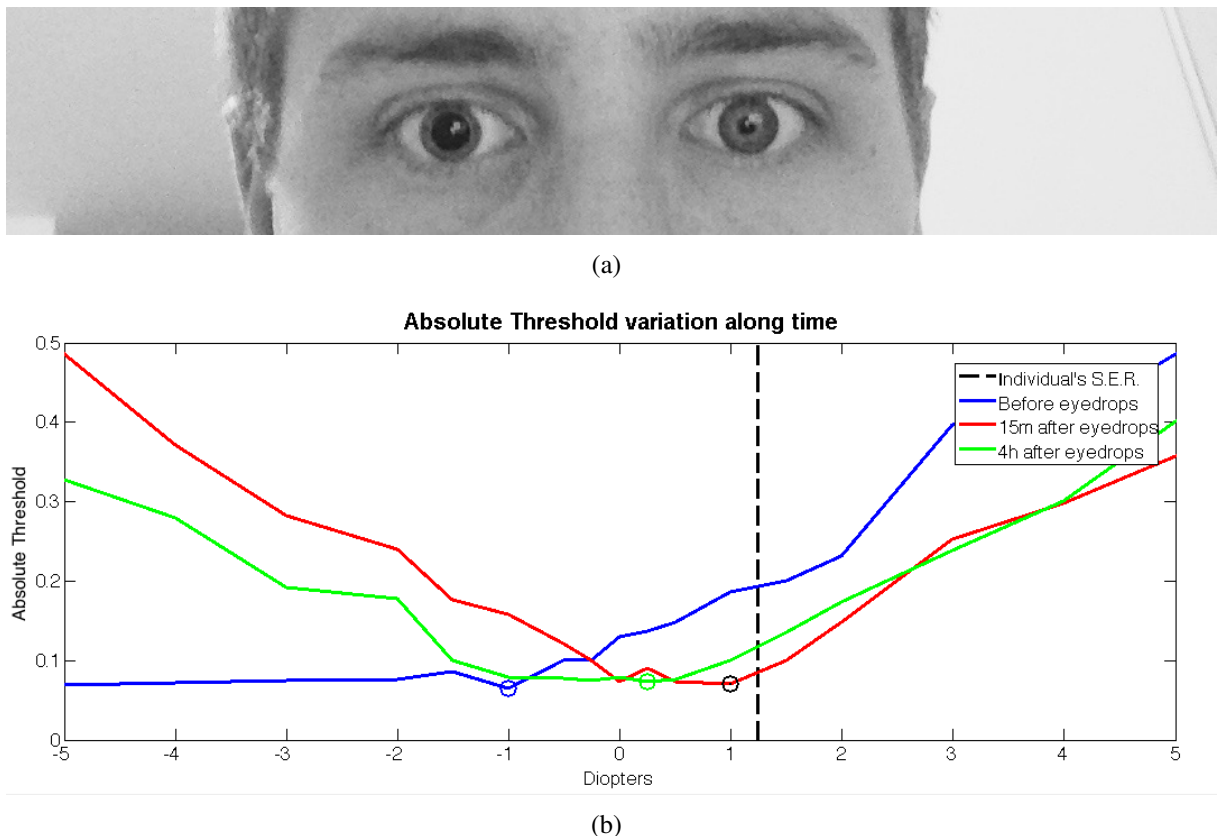


Figure 5.8 – Accommodation analysis. (a) a photo of an eye with the cycloplegic eye drops' effects; (b) plot of some absolute threshold evaluations before and after the use of eye drops.

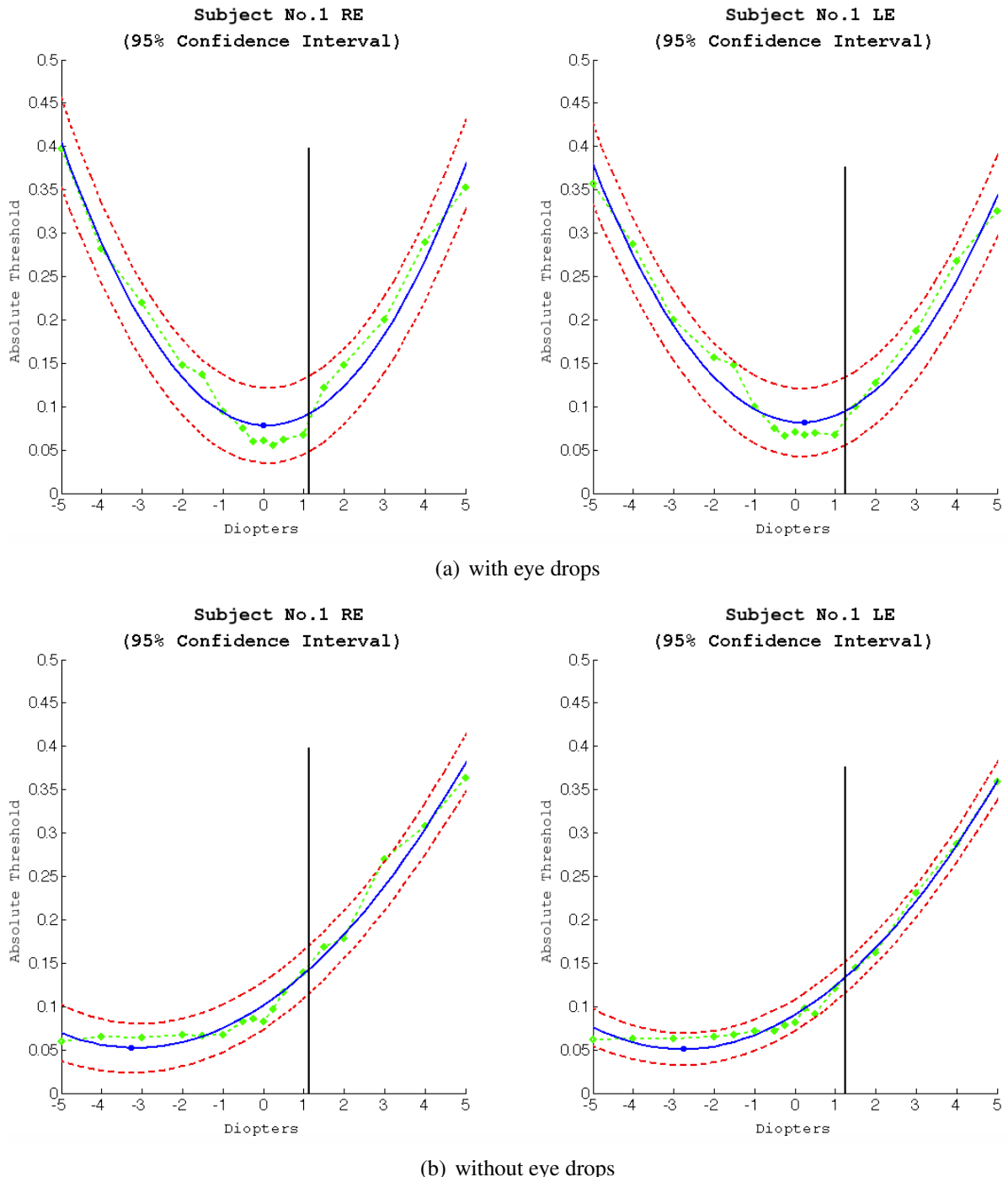


Figure 5.9 – Polynomial fitting of the absolute threshold values of Subject 1. Red lines define the confidence interval of 95%. Green plot points the minimum value for a specific extra lens power, and the blue lines represent the best polynomial fitting highlighting its minor value.

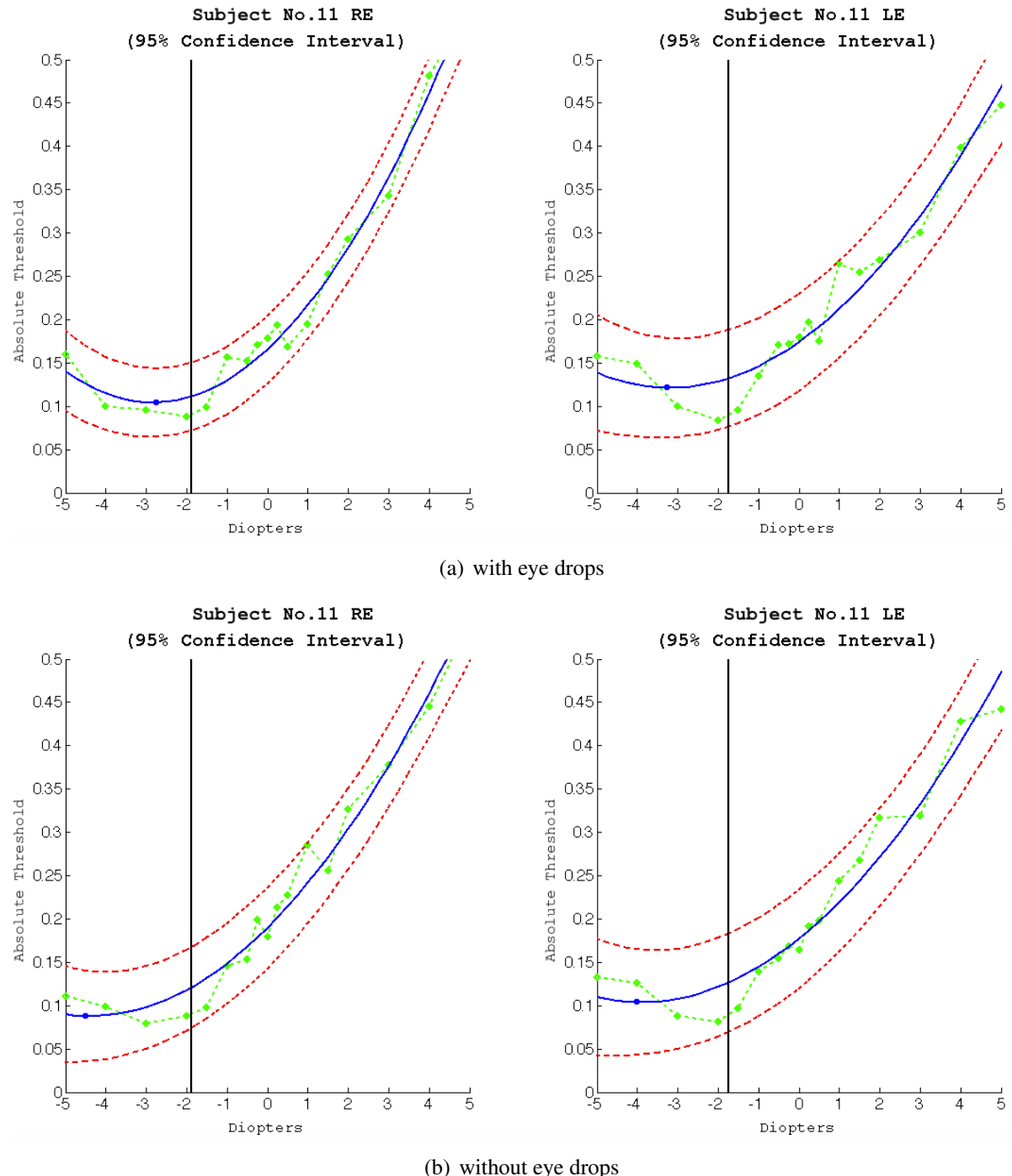


Figure 5.10 – Polynomial fitting of the absolute threshold values of Subject 11. Red lines define the confidence interval of 95%. Green plot points the minimum value for a specific extra lens power, and the blue lines represent the best polynomial fitting highlighting its minor value.

6 CONCLUSION

This thesis presented a technique capable of simulating the perception of monochromatic images when considering optical systems with visual aberrations. It relies on the assumption of a fixed depth and uses Fourier Tools and a DSLR camera to simulate and validate how such aberrations affect vision. Although our solution is able to take into account high-order aberrations, our focus was on not relying on the availability of expensive equipment, such as Shack-Hartmann wavefront sensors. For this, we have focused on estimating the low-order aberrations (*i.e.*, myopia, hyperopia and astigmatism) of ones optical systems and validating the results with an optical ground truth.

We demonstrate its effectiveness by comparing the 40 simulation outcomes with optical ground truths using three objective metrics. Histograms of two of these metrics are presented in Figure 6.1. Note that all SSIM values remains between 0.9119 and 0.9869 (where, $\bar{x} = 0.9313$ and $\sigma = 0.0202$), indicating that our simulations indeed produces results that are structurally very similar the ground truth. Regarding the PSNR metric, values varies from 29.5003 to 39.3720 (where, $\bar{x} = 35.5026$ and $\sigma = 2.1415$). Such PSNR values, given in decibels, indicates that the simulation outcomes are indistinguishable from the optical ground truth captured by the camera.

The absolute threshold psychophysical experiment allowed us to assess its use in order to estimate the spherical equivalent error of an optical system. However, due to its variability and the high number of eye drops necessary to guarantee no crystalline lens' accommodation, we could not find such relation.

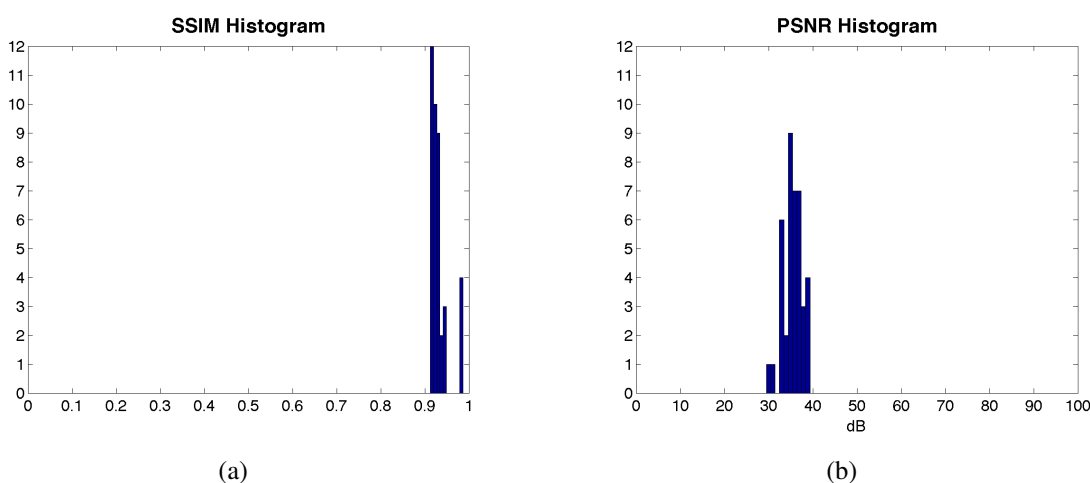


Figure 6.1 – Histogram of SSIM (a) and PSNR (b)

6.1 Future Work

Because visual blurring is a depth-dependent phenomenon, we would like to capture image and depth information from the environment and generate real-time simulations of how low-order aberrations affect the perception of it. Also, we suppose that, by assuming additional information from the individuals in simulations (*e.g.*, absolute threshold), the final result could be hugely improved. In a way that, for example, we could generate images or design displays focusing on intrinsic perception, which cannot be corrected with ordinary eyeglasses.

It would be interesting to study the best objective metric to compare results. Also, for qualitative validation, we intend to simulate the visual perception of a number of subjects who use eyeglasses. And ask the subjects to observe several scenes without using their eyeglasses, as well as to observe the simulated views with eyeglasses on. By doing this, they could indicate how well the simulation approximates their actual vision.

REFERENCES

- BAILEY, I.; LOVIE, J. New design principles for visual acuity letter charts. **American journal of optometry and physiological optics**, v. 53, n. 11, p. 740—745, November 1976. ISSN 0093-7002. Available from Internet: <<http://europepmc.org/abstract/MED/998716>>.
- BARSKY, B. A. Vision-realistic rendering: Simulation of the scanned foveal image from wavefront data of human subjects. In: **Proceedings of the 1st Symposium on Applied Perception in Graphics and Visualization**. New York, NY, USA: ACM, 2004. (APGV '04), p. 73–81. ISBN 1-58113-914-4. Available from Internet: <<http://doi.acm.org/10.1145/1012551.1012564>>.
- BLAKE, R.; SEKULER, R. **Perception**. 5. ed. New York, NY, USA: McGraw-Hill Humanities/Social Sciences/Languages, 2005.
- CAMP, J.; MAGUIRE, L.; ROBB, R. An efficient ray tracing algorithm for modeling visual performance from corneal topography. In: **Visualization in Biomedical Computing, 1990., Proceedings of the First Conference on**. [S.l.: s.n.], 1990. p. 278–285.
- DAI, G.-m. **Wavefront Optics for Vision Correction**. Bellingham, Washington USA: SPIE PRESS, 2008.
- DEERING, M. F. A photon accurate model of the human eye. **ACM Trans. Graph.**, ACM, New York, NY, USA, v. 24, n. 3, p. 649–658, jul 2005. ISSN 0730-0301. Available from Internet: <<http://doi.acm.org/10.1145/1073204.1073243>>.
- DIAS-SANTOS, A. et al. Higher order aberrations in amblyopic children and their role in refractory amblyopia. **Revista Brasileira de Oftalmologia**, SciELO Brasil, v. 73, p. 358–362, 12 2014. ISSN 0034-7280. Available from Internet: <http://www.scielo.br/scielo.php?script=sci_arttext&pid=S0034-72802014000600358&nrm=iso>.
- GLYTSIS, E. N. Example of a simple optical system. Class Note. 2014.
- GOODMAN, J. W. **Introduction to Fourier optics**. 3. ed. Englewood: Roberts and Company Publishers, 2005.
- HUANG, F.-C. et al. Correcting for optical aberrations using multilayer displays. **ACM Trans. Graph.**, ACM, New York, NY, USA, v. 31, n. 6, p. 185:1–185:12, nov 2012. ISSN 0730-0301. Available from Internet: <<http://doi.acm.org/10.1145/2366145.2366204>>.
- HUANG, F.-C. et al. Eyeglasses-free display: Towards correcting visual aberrations with computational light field displays. **ACM Trans. Graph.**, ACM, New York, NY, USA, v. 33, n. 4, p. 59:1–59:12, jul. 2014. ISSN 0730-0301. Available from Internet: <<http://doi.acm.org/10.1145/2601097.2601122>>.
- KING, L. A. **Experience Psychology**. 2. ed. [S.l.]: McGraw-Hill Education, 2012.
- KLEIN, S. A. Measuring, estimating, and understanding the psychometric function: a commentary. **Perception & Psychophysics**, v. 63, p. 1421–1455, 2001.

- KOLB, C.; MITCHELL, D.; HANRAHAN, P. A realistic camera model for computer graphics. In: **Proceedings of the 22Nd Annual Conference on Computer Graphics and Interactive Techniques**. New York, NY, USA: ACM, 1995. (SIGGRAPH '95), p. 317–324. ISBN 0-89791-701-4. Available from Internet: <<http://doi.acm.org/10.1145/218380.218463>>.
- KRONBAUER, A. L. et al. Vision measurement in candelas: description of a psychophysical technique to quantify luminous intensity. **Arquivos brasileiros de oftalmologia**, v. 74, n. 2, p. 91—96, 2011. ISSN 0004-2749. Available from Internet: <<http://dx.doi.org/10.1590/S0004-27492011000200004>>.
- LEEK, M. R. Adaptive procedures in psychophysical research. **Perception & Psychophysics**, v. 63, n. 8, p. 1279–1292, 2001.
- LEMMA, G. General psychology. Lecture Notes. 2005.
- LIANG, J. et al. Objective measurement of wave aberrations of the human eye with the use of a hartmann–shack wave-front sensor. **J. Opt. Soc. Am. A**, OSA, v. 11, n. 7, p. 1949–1957, Jul 1994. Available from Internet: <<http://josaa.osa.org/abstract.cfm?URI=josaa-11-7-1949>>.
- MACHADO, G. M.; OLIVEIRA, M.; FERNANDES, L. A. A physiologically-based model for simulation of color vision deficiency. **Visualization and Computer Graphics, IEEE Transactions on**, v. 15, n. 6, p. 1291–1298, Nov 2009. ISSN 1077-2626.
- MEISTER, D. Wavefront aberrations and spectacle lenses: part one. **Association of British Dispensing Opticians**, p. 6, 2010.
- MOLLON, J. **The origins of modern color science**. 2. ed. Oxford, UK: Elsevier, 2003.
- MONTALTO, C. et al. A total variation approach for customizing imagery to improve visual acuity. **ACM Trans. Graph.**, ACM, New York, NY, USA, v. 34, n. 3, p. 28:1–28:16, may 2015. ISSN 0730-0301. Available from Internet: <<http://doi.acm.org/10.1145/2717307>>.
- MOSTAFAWY, S.; KERMANI, O.; LUBATSCHOWSKI, H. Virtual eye: retinal image visualization of the human eye. **Computer Graphics and Applications, IEEE**, v. 17, n. 1, p. 8–12, Jan 1997. ISSN 0272-1716.
- PAMPLONA, V. F. et al. Netra: Interactive display for estimating refractive errors and focal range. **ACM Trans. Graph.**, ACM, New York, NY, USA, v. 29, n. 4, p. 77:1–77:8, 7 2010. ISSN 0730-0301. Available from Internet: <<http://doi.acm.org/10.1145/1778765.1778814>>.
- PAMPLONA, V. F. et al. Tailored displays to compensate for visual aberrations. **ACM Trans. Graph.**, v. 31, n. 4, p. 81, 2012.
- PAMPLONA, V. F.; OLIVEIRA, M. M.; BARANOSKI, G. V. G. Photorealistic models for pupil light reflex and iridal pattern deformation. **ACM Trans. Graph.**, ACM, New York, NY, USA, v. 28, n. 4, p. 106:1–106:12, sep 2009. ISSN 0730-0301. Available from Internet: <<http://doi.acm.org/10.1145/1559755.1559763>>.
- PAMPLONA, V. F. et al. Catra: Interactive measuring and modeling of cataracts. In: **ACM SIGGRAPH 2011 Papers**. New York, NY, USA: ACM, 2011. (SIGGRAPH '11), p. 47:1–47:8. ISBN 978-1-4503-0943-1. Available from Internet: <<http://doi.acm.org/10.1145/1964921.1964942>>.

- PELLI, D.; ROBSON, J. et al. The design of a new letter chart for measuring contrast sensitivity. In: **Clinical Vision Sciences**. [S.l.]: Raphael's Ltd, London, 1988.
- POTMESIL, M.; CHAKRAVARTY, I. A lens and aperture camera model for synthetic image generation. **ACM SIGGRAPH Computer Graphics**, ACM, v. 15, n. 3, p. 297–305, 1981.
- RITSCHEL, T. et al. Temporal glare: Real-time dynamic simulation of the scattering in the human eye. **Computer Graphics Forum**, Blackwell Publishing Ltd, v. 28, n. 2, p. 183–192, 2009. ISSN 1467-8659. Available from Internet: <<http://dx.doi.org/10.1111/j.1467-8659.2009.01357.x>>.
- SACEK, V. **Monochromatic Eye Aberrations**. 2015. Available from Internet: <http://www.telescope-optics.net/monochromatic_eye_aberrations.htm>.
- SCHWARTZ, S. H. **Visual perception: A clinical orientation**. 4. ed. New York, NY, USA: McGraw-Hill Medical Pub. Division, 2010.
- SCHWIEGERLING, J. **Field Guide to Visual and Ophthalmic Optics**. [S.l.]: SPIE press Bellingham, WA, 2004. (SPIE Field Guides, FG04).
- SMITH, A. **PSFs in IDL**. 2015. Available from Internet: <<http://www.enkaptic.co.uk/2009/03/18/psfs-in-idl/>>.
- THIBOS, L. N. et al. Standards for reporting the optical aberrations of eyes. **Journal of refractive surgery**, Slack Incorporated, v. 18, n. 5, p. S652–S660, 2002.
- THIBOS, L. N.; THIBOS, C. A. Geometrical optical analysis of defocused retinal images to compute the size of retinal blur circles relative to object size. **US Ophthalmic Review**, v. 4, n. 2, p. 104–106, 7 2011.
- TKACZYK, T. S. **Field Guide to Microscopy**. [S.l.]: SPIE press Bellingham, WA, 2010. (SPIE Field Guides, FG13).
- TREUTWEIN, B. Adaptive psychophysical procedures. **Vision Research**, v. 17, n. 1503-2522, 1995.
- WANG, Z. et al. Image quality assessment: from error visibility to structural similarity. **Image Processing, IEEE Transactions on**, v. 13, n. 4, p. 600–612, April 2004. ISSN 1057-7149.
- WATSON, A. B.; AHUMADA JR, A. J. Predicting visual acuity from wavefront aberrations. **Journal of Vision**, v. 8, n. 4, p. 17, 2008. Available from Internet: <<http://dx.doi.org/10.1167/8.4.17>>.
- WHO. **Global Initiative for thw Elimination of Avoidable Blindness: action plan 2006-2011**. [S.l.], 2007.
- YODER, P. R.; VUKOBRAТОVICH, D. **Field Guide to Binoculars and Scopes**. [S.l.]: SPIE press Bellingham, WA, 2011. (SPIE Field Guides, FG19).
- YU, W. M. **Simulation of Vision through an Actual Human Optical System**. Thesis (PhD) — University of California, Berkeley, 2001.
- ZIMBARDO, P. G.; JOHNSON, R. L.; MCCANN, V. **Psychology: core concepts**. 7. ed. New York, NY, USA: Pearson Education, 2012.

APPENDIX A — INDIVIDUAL PARTICIPANT DATA

This appendix contains data captured through the experiments described in Section 5.1. The following participant data is related to the subject with ID number 001. The complete database describing the results can be downloaded at:

http://www.inf.ufrgs.br/~mlkrueger/MSc_Dissertation/IPD_Database.zip

ID Number

Subject identification number

REF. DATA

Examination reference data

EYE DROPS

Whether cycloplegic eye drop was used or not

VD

Vertex distance configured in the TOPCON KR-8900 Autorefractor device

CYL

Cylinder notation (Brazilian notation is the negative one)

PD

Pupil distance

S

Spherical

C

Cylindrical

A

Cylindrical axis

S.E.

Spherical Equivalent ($SE = S + (C/2)$)

MV

Minimum visible

ET

Elapsed time

LM

Lux Mean



IPD - Individual Participant Data

ID Number: 001**Birthdate:** 13/03/1990**KR-8900****Gender:** Male**TOPCON**

REF. DATA		27/11/2014	
EYE DROPS		[X] YES [] NO	
VD	CYL	PD	
12.00	(-)	61	
< RIGHT EYE >			
S	C	A	S.E.
+ 1,25	- 0,25	7	+ 1,13
< LEFT EYE >			
S	C	A	S.E.
+ 1,25	0,00	0	+ 1,25

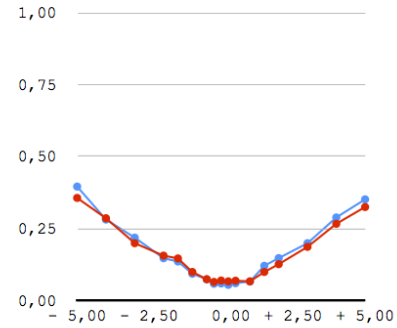
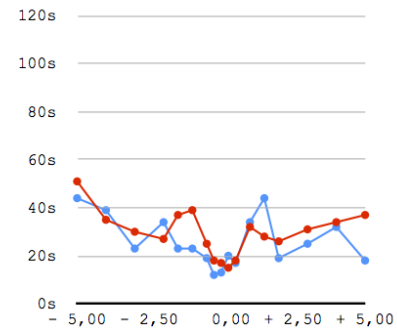
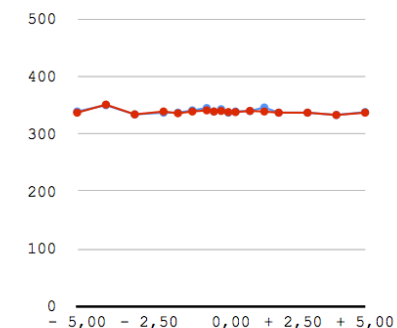
REF. DATA		27/11/2014	
EYE DROPS		[] YES [X] NO	
VD	CYL	PD	
12.00	(-)	61	
< RIGHT EYE >			
S	C	A	S.E.
+ 0,50	- 0,25	6	+ 0,38
< LEFT EYE >			
S	C	A	S.E.
+ 0,75	- 0,25	2	+ 0,63

MATLAB Random Sequences

1st Examination	2nd Examination	3rd Examination	4th Examination
- 1,50	+ 1,50	- 0,25	+ 3,00
+ 1,00	+ 4,00	- 3,00	+ 2,00
+ 1,50	- 0,50	+ 1,00	+ 1,50
- 4,00	- 4,00	- 2,00	- 0,50
- 0,50	+ 1,00	- 5,00	- 1,50
0,00	- 0,25	+ 3,00	0,00
- 1,00	- 1,50	+ 1,50	- 3,00
+ 3,00	+ 0,50	+ 0,25	+ 5,00
- 2,00	+ 2,00	- 4,00	- 0,25
+ 0,50	- 1,00	+ 4,00	- 5,00
+ 2,00	0,00	+ 5,00	- 4,00
- 3,00	+ 5,00	- 0,50	+ 0,25
+ 4,00	+ 3,00	+ 0,50	+ 1,00
+ 5,00	- 2,00	+ 2,00	- 1,00
+ 0,25	+ 0,25	- 1,50	+ 0,50
- 0,25	- 5,00	0,00	- 2,00
- 5,00	- 3,00	- 1,00	+ 4,00

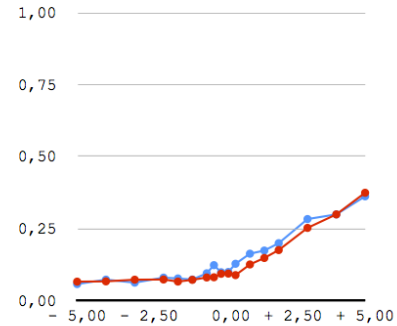
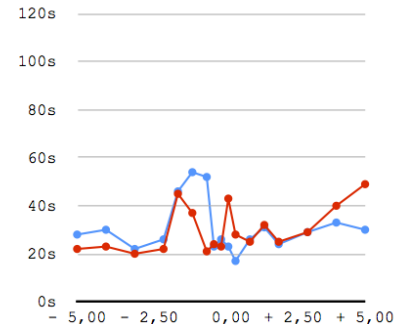
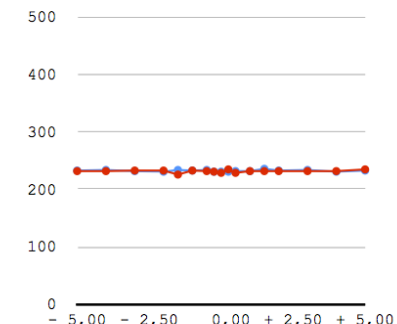
ID Number: 001**REF. DATA:** 27/11/2014**Birthdate:** 13/03/1990**EYE DROPS:** YES**Gender:** Male**DURATION:** 15m 39s**1st Examination**

Diopter	Eye	MV	ET	LM
+ 5,00	<R>	0,3522	18s	338 lx
	<L>	0,3256	37s	337 lx
+ 4,00	<R>	0,2894	32s	333 lx
	<L>	0,2674	34s	333 lx
+ 3,00	<R>	0,2000	25s	337 lx
	<L>	0,1872	31s	337 lx
+ 2,00	<R>	0,1481	19s	337 lx
	<L>	0,1271	26s	337 lx
+ 1,50	<R>	0,1215	44s	346 lx
	<L>	0,1000	28s	339 lx
+ 1,00	<R>	0,0669	34s	340 lx
	<L>	0,0674	32s	340 lx
+ 0,50	<R>	0,0611	17s	339 lx
	<L>	0,0696	18s	338 lx
+ 0,25	<R>	0,0553	20s	337 lx
	<L>	0,0674	15s	338 lx
0,00	<R>	0,0601	13s	343 lx
	<L>	0,0703	17s	340 lx
- 0,25	<R>	0,0592	12s	339 lx
	<L>	0,0655	18s	339 lx
- 0,50	<R>	0,0744	19s	345 lx
	<L>	0,0749	25s	341 lx
- 1,00	<R>	0,0940	23s	341 lx
	<L>	0,1000	39s	339 lx
- 1,50	<R>	0,1365	23s	337 lx
	<L>	0,1471	37s	336 lx
- 2,00	<R>	0,1478	34s	337 lx
	<L>	0,1568	27s	339 lx
- 3,00	<R>	0,2193	23s	334 lx
	<L>	0,2000	30s	334 lx
- 4,00	<R>	0,2821	39s	350 lx
	<L>	0,2867	35s	351 lx
- 5,00	<R>	0,3966	44s	339 lx
	<L>	0,3572	51s	337 lx

○ <R> ● <L>
Minimum Visible**Elapsed Time****Lux Mean**

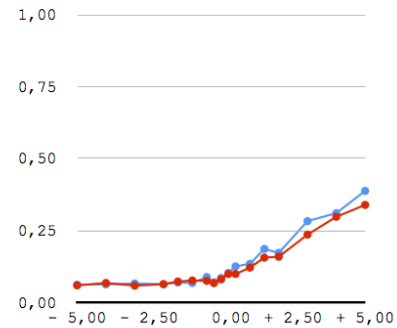
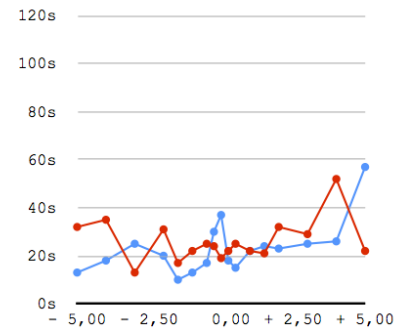
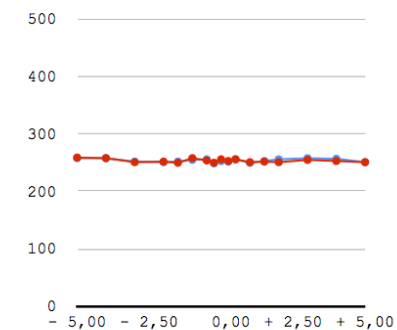
ID Number: 001**REF. DATA:** 11/11/2014**Birthdate:** 13/03/1990**EYE DROPS:** NO**Gender:** Male**DURATION:** 17m 8s**2nd Examination**

Diopter	Eye	MV	ET	LM
+ 5,00	<R>	0,3628	30s	233 lx
	<L>	0,3751	49s	235 lx
+ 4,00	<R>	0,3000	33s	231 lx
	<L>	0,3000	40s	232 lx
+ 3,00	<R>	0,2838	29s	234 lx
	<L>	0,2531	29s	232 lx
+ 2,00	<R>	0,2000	24s	233 lx
	<L>	0,1761	25s	232 lx
+ 1,50	<R>	0,1744	31s	236 lx
	<L>	0,1486	32s	232 lx
+ 1,00	<R>	0,1635	26s	232 lx
	<L>	0,1261	25s	232 lx
+ 0,50	<R>	0,1285	17s	232 lx
	<L>	0,0891	28s	229 lx
+ 0,25	<R>	0,1000	23s	231 lx
	<L>	0,0944	43s	235 lx
0,00	<R>	0,0990	26s	231 lx
	<L>	0,0937	23s	229 lx
- 0,25	<R>	0,1237	23s	231 lx
	<L>	0,0816	24s	231 lx
- 0,50	<R>	0,0954	52s	234 lx
	<L>	0,0809	21s	232 lx
- 1,00	<R>	0,0737	54s	233 lx
	<L>	0,0727	37s	233 lx
- 1,50	<R>	0,0775	46s	234 lx
	<L>	0,0667	45s	226 lx
- 2,00	<R>	0,0804	26s	231 lx
	<L>	0,0739	22s	233 lx
- 3,00	<R>	0,0630	22s	232 lx
	<L>	0,0732	20s	233 lx
- 4,00	<R>	0,0734	30s	234 lx
	<L>	0,0674	23s	232 lx
- 5,00	<R>	0,0580	28s	233 lx
	<L>	0,0664	22s	232 lx

○ <R> ● <L>
Minimum Visible**Elapsed Time****Lux Mean**

ID Number: 001**REF. DATA:** 13/11/2014**Birthdate:** 13/03/1990**EYE DROPS:** NO**Gender:** Male**DURATION:** 13m 56s**3rd Examination**

Diopter	Eye	MV	ET	LM
+ 5,00	<R>	0,3886	57s	251 lx
	<L>	0,3399	22s	251 lx
+ 4,00	<R>	0,3114	26s	257 lx
	<L>	0,2986	52s	253 lx
+ 3,00	<R>	0,2836	25s	258 lx
	<L>	0,2367	29s	255 lx
+ 2,00	<R>	0,1734	23s	256 lx
	<L>	0,1599	32s	251 lx
+ 1,50	<R>	0,1870	24s	253 lx
	<L>	0,1568	21s	252 lx
+ 1,00	<R>	0,1353	22s	250 lx
	<L>	0,1220	22s	251 lx
+ 0,50	<R>	0,1263	15s	256 lx
	<L>	0,1000	25s	256 lx
+ 0,25	<R>	0,1036	18s	252 lx
	<L>	0,1000	22s	253 lx
0,00	<R>	0,0862	37s	253 lx
	<L>	0,0812	19s	256 lx
- 0,25	<R>	0,0710	30s	249 lx
	<L>	0,0681	24s	250 lx
- 0,50	<R>	0,0894	17s	256 lx
	<L>	0,0761	25s	254 lx
- 1,00	<R>	0,0686	13s	255 lx
	<L>	0,0775	22s	258 lx
- 1,50	<R>	0,0703	10s	252 lx
	<L>	0,0739	17s	250 lx
- 2,00	<R>	0,0645	20s	251 lx
	<L>	0,0645	31s	252 lx
- 3,00	<R>	0,0671	25s	252 lx
	<L>	0,0594	13s	251 lx
- 4,00	<R>	0,0638	18s	258 lx
	<L>	0,0688	35s	258 lx
- 5,00	<R>	0,0626	13s	258 lx
	<L>	0,0604	32s	259 lx

○ <R> ● <L>
Minimum Visible**Elapsed Time****Lux Mean**

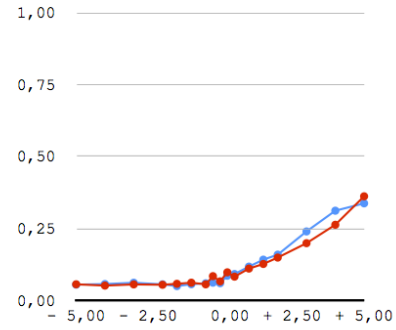
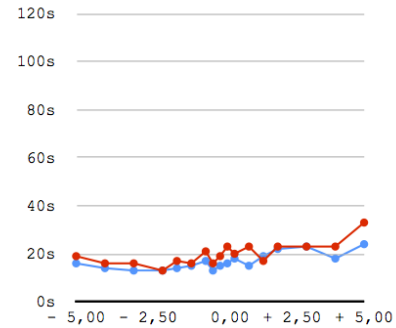
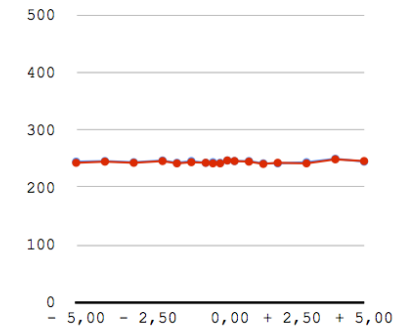


IPD - Individual Participant Data

ID Number: 001**REF. DATA:** 14/11/2014**Birthdate:** 13/03/1990**EYE DROPS:** NO**Gender:** Male**DURATION:** 10m 23s**4th Examination**

Diopter	Eye	MV	ET	LM
+ 5,00	<R>	0,3384	24s	245 lx
	<L>	0,3628	33s	246 lx
+ 4,00	<R>	0,3128	18s	250 lx
	<L>	0,2640	23s	249 lx
+ 3,00	<R>	0,2408	23s	244 lx
	<L>	0,2000	23s	242 lx
+ 2,00	<R>	0,1601	22s	242 lx
	<L>	0,1500	23s	243 lx
+ 1,50	<R>	0,1428	19s	242 lx
	<L>	0,1278	17s	241 lx
+ 1,00	<R>	0,1186	15s	246 lx
	<L>	0,1118	23s	245 lx
+ 0,50	<R>	0,0928	18s	246 lx
	<L>	0,0838	20s	246 lx
+ 0,25	<R>	0,0870	16s	247 lx
	<L>	0,0988	23s	247 lx
0,00	<R>	0,0611	15s	243 lx
	<L>	0,0674	19s	242 lx
- 0,25	<R>	0,0628	13s	244 lx
	<L>	0,0855	16s	242 lx
- 0,50	<R>	0,0606	17s	243 lx
	<L>	0,0570	21s	243 lx
- 1,00	<R>	0,0575	15s	246 lx
	<L>	0,0628	16s	244 lx
- 1,50	<R>	0,0510	14s	243 lx
	<L>	0,0589	17s	242 lx
- 2,00	<R>	0,0570	13s	247 lx
	<L>	0,0556	13s	246 lx
- 3,00	<R>	0,0626	13s	244 lx
	<L>	0,0568	16s	243 lx
- 4,00	<R>	0,0580	14s	246 lx
	<L>	0,0527	16s	245 lx
- 5,00	<R>	0,0560	16s	245 lx
	<L>	0,0572	19s	243 lx

○ <R> ● <L>

Minimum Visible**Elapsed Time****Lux Mean**

ID Number: 001*Analysis of the data captured without eye drops***Birthdate:** 13/03/1990**Gender:** Male